Montanuniversität Leoben

PVD TiAlN/CrAlN Multilayer Systems for Cutting Applications

Diploma Thesis

by

Tamara Teppernegg
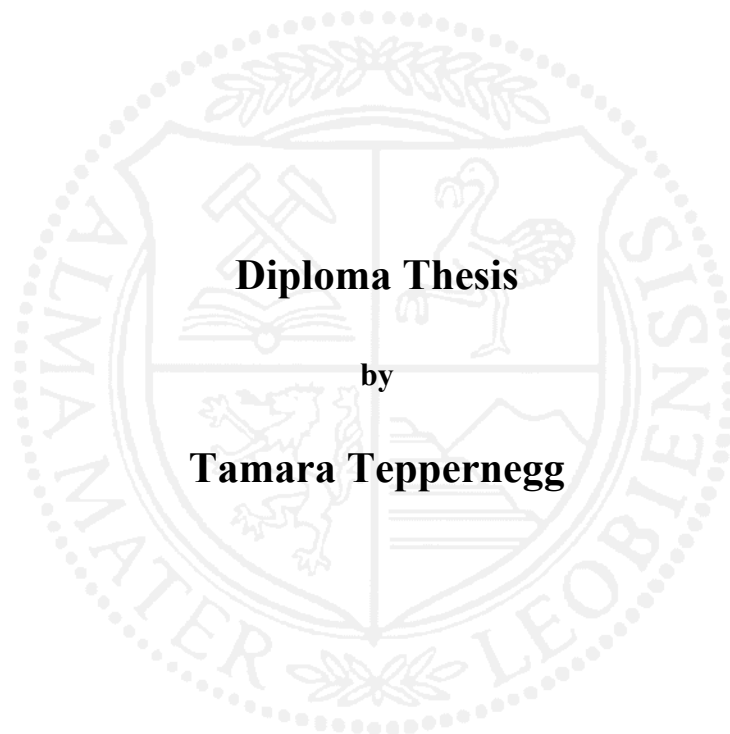
This work has been carried out in cooperation with CERATIZIT Austria G.m.b.H., CERATIZIT Luxembourg S.à.r.l. and at the Department of Physical Metallurgy and Materials Testing, Montanuniversität Leoben

Leoben, 12.03.2012

Affidavit:

I declare in lieu of oath, that I wrote this thesis and performed the associated research myself, using only literature cited in the volume.

Leoben, 12.03.2012   Signature, Candidate

Acknowledgment

1 Introduction

Tools for severe cutting applications are often made of cemented carbide. To increase their performance and lifetime, they may be coated with hard coatings [1-3]. These coatings are produced by either chemical (CVD) or physical vapor deposition (PVD) [1, 4]. During the cutting process, the temperature between the cutting insert and the workpiece material may reach more than 1000 °C [4, 3]. An optimized material for these inserts should show a high hardness, a high thermal stability, high oxidation resistance and low wear rate [3]. State of the art for high speed cutting processes are coatings based on TiAlN. Most of these TiAlN coatings are deposited by the PVD process of cathodic arc evaporation [4, 5]. Further improvement of these coatings can be achieved by multilayer architectures [6-11]. In particular, TiAlN coatings in combination with Ta doped TiAlN has been shown to yield promising results [5]. TiAlN coatings start to oxidize at temperatures above 700 °C [12], whereas CrAlN as an alternative coating material shows excellent oxidation resistance up to 1000 °C [13, 14].

Thus, the aim of this work was to develop and evaluate multilayer arrangements based on TiAlN and CrAlN layers. Special emphasis was laid on the variation of the Al content in the TiAlN and CrAlN layers as well as on the effect of layer thickness. The deposited multilayer coatings have been investigated with respect to their chemical composition, microstructure, mechanical and tribological properties as well as thermal stability. In addition, their performance was evaluated in dry milling tests of quenched and tempered steel. A presently industrially applied multilayered coating based on TiAlN and TiAlTaN layers was used for comparison of the application potential of the coatings developed within this thesis.

2   Theoretical Background

2.1   PVD Techniques

The main physical vapour deposition methods sputtering and evaporation, especially cathodic arc evaporation (CAE) which is used in this work, and the growth mechanisms of thin films are described in this chapter. A particular part of this thesis is devoted to CAE and how to influence the growth of thin films by changing the deposition condition which results in a change of structure and morphology of the coatings.

2.1.1 General

Physical vapor deposition (PVD) is a method to apply coatings for a large number of applications, from decorative films for architectural applications, thin films for semiconductor industries to hard coatings for tool protection. PVD coating thicknesses range from a few nanometers to several ten microns, using deposition temperatures up to 700 °C. Two different techniques are the dominant processes, i.e. sputtering and evaporation, which are illustrated in Fig. 1. They differ in the method how the cathode material, the so called target, is vaporized [1, 15-18].

a)   b)
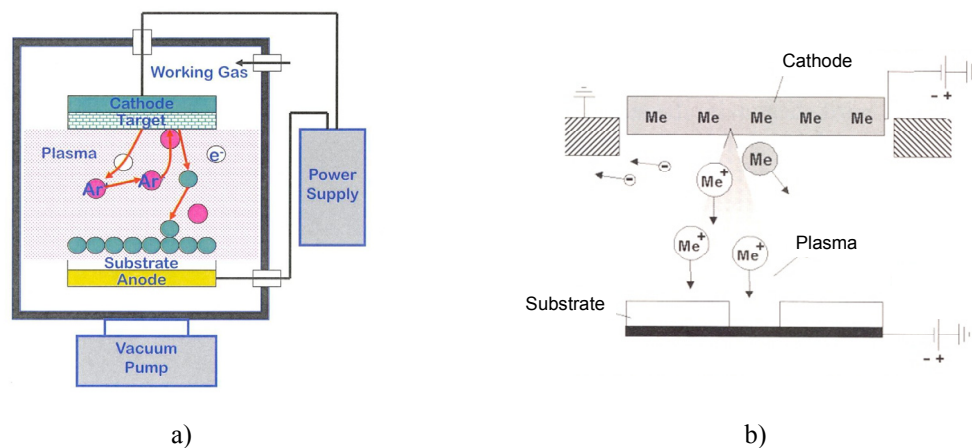
Fig. 1: a) Schematic drawing of the basic PVD techniques: sputtering [4], **b)** evaporation [1]

In the **sputter process** the target is the cathode and the substrate, the material to be coated, is the anode. A negative voltage is applied on the target, which ignites a glow discharge ionizing the Ar working gas. For producing different film compositions, e.g. nitrides or oxides, the working gas can be mixed with N or O. The Ar^+ ions are accelerated towards the target and when their energy is high enough, they vaporize the atoms of the target. The vapor of the target, which consists of typically neutral atoms, condenses on the substrate surface. Sputtered coatings show good adhesion but the deposition rates are rather low e.g. $< 10^{-10}$ m/sec, compared to evaporation [1, 15, 16, 19].

In the **evaporation process,** the target material is vaporized by the input of thermal energy via different methods. The material can be heated in a crucible, either by resistance or induction, by an electron or laser beam or by arcs. The vapor phase consists mostly of neutral particles and a very small fraction of ions [1]. For the deposition process a vacuum of better than 10^{-7} to 10^{-13} bar is necessary to have a collision free path between target and substrate for the particles [15]. Advantages of evaporation compared to sputtering are the higher possible deposition rates combined with satisfactory adhesion. The disadvantages are rather inhomogeneous deposition, difficulties of composition control and the low kinetic energy of the arriving atoms. These energies are ~2 eV and 10-100 eV for the evaporation process and the sputtering process, respectively. The increasing kinetic energy of the arriving atoms is beneficial for the coating properties [1, 4]. This led to development of **ion plating**. Here the substrate has a negative potential. Further, the atoms from the target are ionized by the plasma and accelerated towards the substrate, causing a constant bombardment during growth of the film. The consequence is improved adhesion, microstructure and deposition rate, while the substrate temperature is rather low [1, 15].

2.1.2 Cathodic Arc Evaporation (CAE)

CAE is one of the most important deposition methods for industrial application because the technique is fast, efficient and cost effective. The target, which is the cathode, is vaporized by an electrode under arcing condition whereas the substrate and the walls of the vacuum chamber are the anode [1, 13, 17, 20, 21]. The process needs a high vacuum with a pressure below 10^{-5} – 10^{-10} bar to avoid collisions during the transport of particles between substrate and target [17]. A high current of around 100 A and low voltage of about 10 V are applied. Due to the roughness of the target surface and consequently the limited size of surface asperities, field electron emission is fostered, which creates an arc. This arc only concentrates on one point of the target surface, that is why it is called arc spot. This spot is 1 to 20 μm in diameter, has a high energy density of 10^7 to 10^9 W/cm² and only exists for 5 to 40 ns [1, 20, 22]. The target material is vaporized immediately explosively and the local pressure increases up to 200 bar. This particle stream called plasma jet is accelerated to the substrate by a negative bias voltage, which is applied between the target and the substrate. The plasma jet maybe ionized up to 100 % [23]. The arc creates a crater in the target, the high field electron emission decreases and the arc extinguishes. At the edge of the crater a new surface peak is developed and a new arc is created and the process begins again [16, 20]. The arc moves randomly. When the target has a disc form, then the arc concentrates statistically in the middle of the disc and the erosion is mostly centered. The arc movement can be controlled with a strong magnet field, which is called steered arc [15, 20]. Due to the high pressure of the plasma jet, also molten particles with a diameter of several μm are created. If they are transported towards the substrate, they cause defects in the coating, the so called droplets. They influence the properties of the coatings negatively due to increased surface roughness,

inhomogeneous structure and composition, which also decrease the hardness of the coating by creating pores [4, 16, 20, 24, 25]. The development of droplets can be minimized by increasing the melting point of the target material, increasing the vapor pressure at the melting point of the cathodic material and further the velocity of the movement of the arc spot can be speeded up. A disadvantage of increasing the speed is the decreasing deposition rate. A further option to reduce the droplets is the use of filters, where electrons and ions are separated from the particles based on the difference of the mass ratio [20, 26].

2.1.3 Growth Mechanisms of Thin Films

The structure of thin films has a significant influence on its properties. The particle flux arrives at the surface and is adsorbed there. Accumulations of atoms called clusters are created by surface diffusion of the adsorbed species. When the clusters exceed the critical size, most of the arrived atoms diffuse to the cluster which consequently grows, as illustrated in Fig. 2 [4].
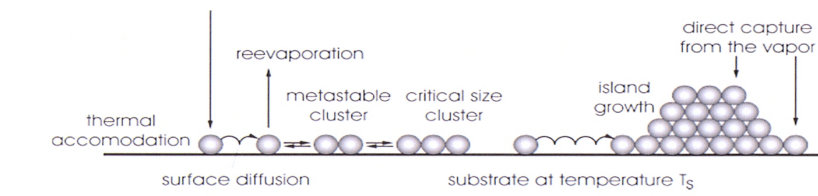
Fig. 2: Process of nucleation and grain growth during deposition process [2]

If the cluster size is too small, it decomposes and the atoms can be desorbed again. The growth of the coating depends highly on the temperature of the substrate surface and the kinetic energy of the arriving atoms. The possible structure developments are shown in Fig. 3. Zero surface diffusion with the same condensation coefficient in all crystal direction creates a structure, which is illustrated in Fig 3 a). This structure is open and porous with high surface roughness. Shadowing is a further effect, which increases porosity. The coating flux does not cover the whole surface or areas behind an obstacle. These areas can only be filled by surface diffusion of neighboring atoms. The structure in Fig. 3 b) is generated without surface diffusion, but with condensation in preferred crystallographic orientation. Fig. 3 c, d) show a dense structure caused by a high surface diffusion. Further the structure, which is illustrated in Fig. 3 d), has a fine grained morphology caused by periodic nucleation during growth [1, 2, 4, 5, 13, 24, 27]. The temperature on the surface, the kinetic energy of the arriving atoms and avoiding the shadowing effect depend on several deposition parameters. In particular, the applied substrate bias voltage influences the ion energy. To avoid the shadowing effect for homogeneous coating deposition, the position of the substrate to the source is crucial [4].

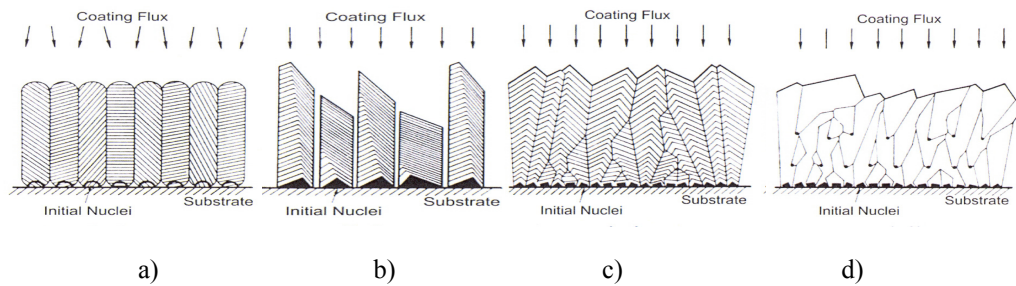a)   b)   c)   d)

Fig. 3: Different growth structures **a)** Growth with unity condensation coefficient, without surface diffusion, **b)** Growth with condensation coefficient in preferred crystallographic orientation, without surface diffusion, **c)** Growth with surface diffusion, **d)** Growth with surface diffusion and periodic nucleation [28]

For supporting the adsorption process, the substrate pre-treatment, that is most often an ion etching process, is very important. The heating process is central for a homogeneous substrate temperature, which is decisive for surface mobility of the atoms. Over the last forty years models have been developed, which try to connect the deposition parameters with the crystal growth independent of the coating material. In 1969 the first structure model, which is illustrated in Fig. 4 a), was developed by Movchan and Demchishin [29]. They investigated the relation between the coating morphology and the homologous temperature T_s/T_m, which is defined by the substrate temperature T_s and melting point T_m of the coating material. At low $T_s/T_m < 0.3$ (zone 1) the atom mobility is very poor and shadowing effect takes place, which causes porous structures with high surface roughness. In zone 2 ($0.3 < T_s/T_m < 0.5$) the atom mobility is higher. Pores, which are created by the shadowing effect, can be filled up. The coating is dense, the grains have a columnar form and the surface looks smooth. With increasing substrate temperature T_s, the grain size increases as is shown for zone 2. At the temperature next to the melting point (zone 3) $0.5 < T_s/T_m < 1$, recrystallization starts already during the deposition process. Now the grains have a coarse and dense structure. Thornton and Messier [28, 30] improved the structure model by adding a third axis including the dependence of the structure on the ambient Argon atmosphere, which is important for the sputtering process. This third axis creates a new zone T, which has properties located between zone 1 and 2. The zone T shows a dense and columnar grain structure, which is created by the increased atom mobility. The surface is very smooth. For sputtering and arc evaporation, Messier improved the concept of Movchan and Demchishin with the bias voltage as third axis [30], which is illustrated in Fig. 4 b). The bias voltage causes an acceleration of the particle flux to the substrate, which influences the morphology of the coating by increasing the kinetic energy of the ions. At low bias voltages the T zone does not exist, whereas at higher voltages the T zone becomes broader and consequently zone 1 gets very small [1, 5, 15, 17, 20].
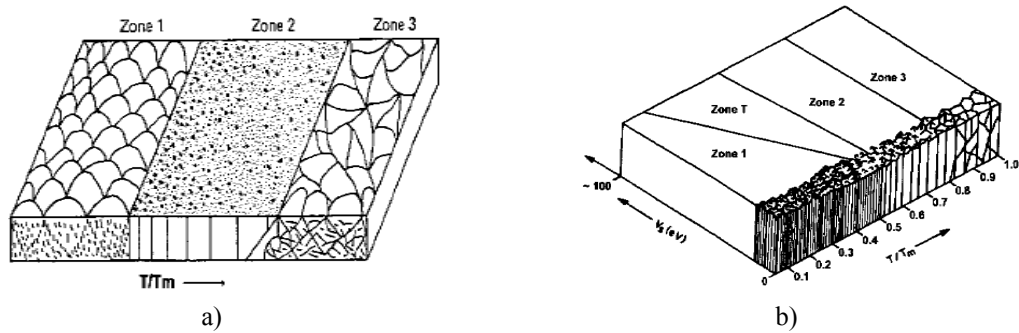
Fig. 4: a) Structure zone model by Movchan and Demchishin [29], **b)** Modified model by Messier [30]

2.2 TiAlN and CrAlN Coating Systems

For cutting processes further tool and coating material improvements like high hardness, abrasive wear resistance and thermal resistance are needed. TiN is used as hard coating on cemented carbide substrates for cutting tools for more than 35 years. It is characterized by a high hardness of ~2300 HV 0.05 and also good toughness [3]. TiN has limited oxidation resistance at temperatures above 500 °C. It oxidizes to TiO_2, which has poor properties for cutting applications. Further, next to TiN CrN coatings are used since the 1980ies, because of their superior corrosion and wear resistance. CrN and TiN may be further improved by alloying with Al [31-38]. Both metastable TiAlN and CrAlN ternary phases show high oxidation resistance and high hardness. Further TiAlN has a low thermal conductivity. Depending on the Al content, TiAlN and CrAlN coatings crystallize in different crystallographic structures. They can consist of a single–phase face centered cubic (fcc) solid solution for lower Al contents. At higher Al contents, the coatings crystallize in dual phase structure of the fcc and the hexagonal close-packed modification (hcp), or as single hcp phase, illustrated in Fig. 5 for CrAlN [12, 33, 39].
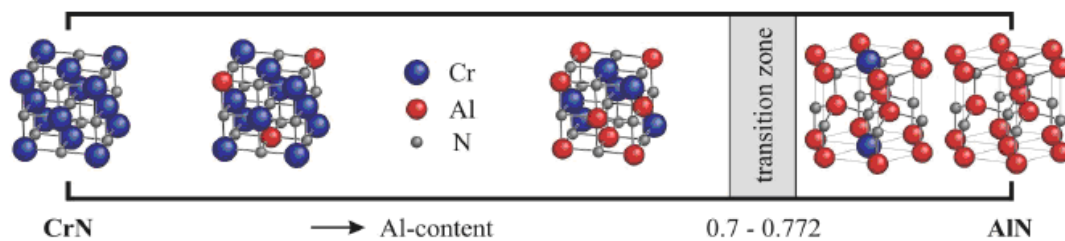
Fig. 5: Crystal structure of CrAlN in dependency of the chemical composition [33]

The area of existence of the fcc $Ti_xAl_{1-x}N$ varies in the literature from 55 mol% to 67 mol% AlN, whereas the existence of the fcc $Cr_xAl_{1-x}N$ is terminated at 71 mol% AlN. Above these values, the hcp modification, which shows inferior mechanical properties than the fcc modification is formed [5, 12, 33, 39-42]. The Al atom is smaller than both the Ti and Cr atoms which causes a decrease of the lattice parameter in the fcc lattice,

e.g. in the TiAlN system from 0.424 nm without AlN, corresponding to TiN, to 0.417 for 60 mol% AlN, as illustrated in Fig. 6 a). Pure CrN has a lattice parameter between 0.414 and 0.416 nm [43, 44], whereas pure fcc AlN has 0.413 nm [33]. The lattice constants of the stable AlN phase show changes with increasing Ti-content and an anisotropic behavior, where the a–axis shrinks and the c-axis expands, which is shown in Fig. 6 b) for the CrAlN system. Due to the lattice misfit, compressive stresses lead to an increase in hardness with increasing Al content. Further, the hardness is improved by changing the bonding structure from the metallic bonding of TiN to the covalent bonding of AlN, often creating a nanocrystalline structure [5, 40, 45-52].

a) b)

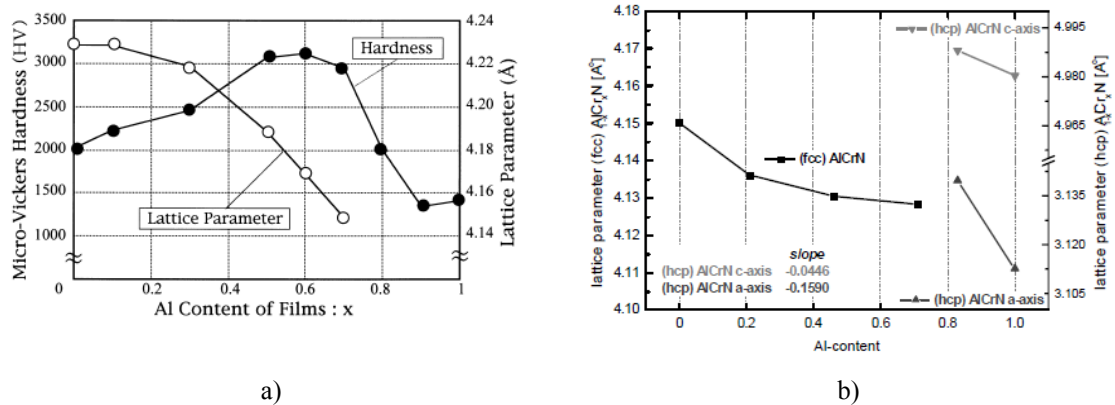**Fig. 6: a)** Hardness and lattice parameter as a function of the Al-content in the TiAlN system [46], **b)** Lattice parameters as function of the Al–content in CrAlN [34]

Kutschej et al. [40] reported for sputtered TiAlN the highest hardness values of 33 GPa at AlN contents of 54 mol%. Fig. 6 a) shows the decreasing hardness with AlN contents increasing above 54 mol% to 19 GPa. The values of the hardness are similar in the literature but the Al content is different, where ~36.5 GPa at an AlN content of 66 mol% [53] and 31.4 GPa at an AlN content of 40 mol% is measured [12, 54, 55]. The micro hardness values of CrAlN reported in the literature vary from 16 GPa to 40 GPa, at room temperature even with the same chemical composition. Further the hardness depends on the bias voltage in the arc evaporation process. With increasing bias voltage the defect density increases, which consequently improves the hardness [31, 34, 56-60]. Different microstructures, measurement methods and divergent measurement parameters are reasons for these deviations. Reiter et al. [34] reported that the maximum hardness of CrAlN is ~38 GPa at 46 mol% AlN whereas the best wear resistance was obtained at an AlN content of 71 mol%. Due to the transformation from the fcc to the hcp structure, the hardness decreases dramatically at AlN contents ≥ 77.2 mol%.

At higher temperature most materials tend to decrease hardness by recovery process, where lattice defects, caused by the deposition process, are annealed out due to the increasing diffusion, and by recrystallization, which starts, e.g. for TiN at 400 °C. Thermal stability is

important for high speed cutting, because there the temperature at the cutting edge can exceed 1000 °C.

TiAlN and CrAlN decompose at higher temperatures, but the hardness is increased by age hardening in the temperature range between 600 and 950 °C. The ongoing reactions can be detected by differential scanning calometry (DSC) as shown for TiAlN in Fig. 7 a). The first reaction (DSC1) starts between 500 and 800 °C and is a recovery process. In the second reaction (DSC2) some TiAlN domains are enriched with fcc AlN, which increases the hardness caused by the formed coherent strains. DSC3 starts at ~900 °C and the coating now consists of three different phases, i.e. the fcc TiAlN matrix, fcc AlN and fcc TiN. The decomposition process is completed after the fourth reaction (DSC4) at 1400 °C. The fcc AlN phase is totally transformed into the stable hcp structure [53, 61-65].

CrAlN decomposes at higher temperatures and above 1230 °C fcc CrAlN does not exist anymore, see Fig. 7 b). A first exothermic reaction is the recovery process and occurring at ~625 °C. At ~900 °C, first hcp AlN precipitations can be detected by XRD. This phase is located at grain boundaries and triple junctions whereas the matrix becomes Cr enriched. Above 1100 °C the Cr-N bonds weaken and nitrogen loss starts. Consequently, the hexagonal Cr_2N is formed. Further, Cr_2N is decomposed into the base cubic centered (bcc) Cr and N_2 gas, which is completed under inert gas atmosphere at 1550 °C. During annealing of hcp AlN, where Cr occupies an Al place, fcc CrN is created and is found at the grain boundary. This CrN also decomposes into hcp Cr_2N and N_2 and further into bcc Cr [33-36]. Between 500 and 1000 °C, which is a common temperature for cutting applications, the increase of hardness is beneficial.
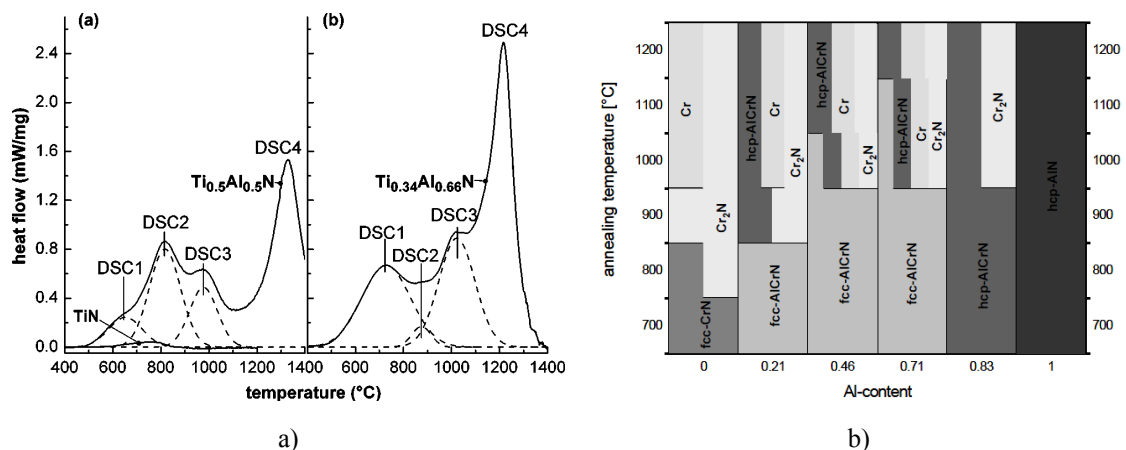
Fig. 7: a) DSC measurements of $Ti_{0.5}Al_{0.5}N$ and $Ti_{0.34}Al_{0.66}N$ [53, 61-63] **b)** schematic phase diagram of AlCrN with different Al contents after annealing at different temperatures in Ar atmosphere [34]

Beside the thermal stability, the oxidation resistance is one of the important properties for cutting tools. For the fcc TiAlN and CrAlN phases, the oxidation resistance increases with increasing Al content [32, 34, 66-71]. The initiation of oxidation of $Ti_{0.8}Al_{0.2}N$ already starts at 700 °C, whereas TiN alloyed with 60-70 mol% AlN is stabled up to ~950 °C, which is

illustrated in Fig. 8. On the TiAlN surface an Al_2O_3 layer, which is very thin, dense and highly insulating, is created, which acts as a diffusion barrier. This layer reduces the oxygen diffusion into the coating and prevents further oxidation. Below the Al_2O_3 layer, a porous TiO_2 layer is formed [66-69].

Fig. 8: Different oxidations curves of TiAlN as function of the Al concentration [12]

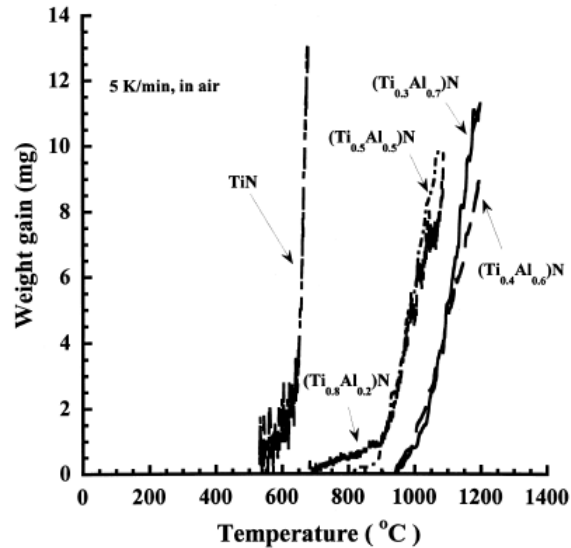Around temperatures of 1000 °C in the CrAlN system, Cr_2O_3 is determined at the surface of CrAlN coatings with low Al content. With increasing Al content Al_2O_3 is also formed next to the Cr_2O_3 on the surface. Similar as TiAlN below the $(Cr, Al)_2O_3$ layer a Cr_2O_3 layer is created. At 46 mol% Al in the coating the oxide layer is very dense and the oxygen atoms are hindered to diffuse into the coating [13, 14, 32, 34, 70].

2.3   Nanosized Multilayers

To combine the properties high hardness and high toughness or high hardness and low coefficient of friction (CoF) in one material is a dream of materials scientists. Nanocomposites provide the opportunity to combine materials with different beneficial properties. Therefore, nanolayered coatings become more and more interesting for cutting applications [6-11]. An important parameter for the characterization of multilayers is the bilayer period or modulation wavelength λ, which describes the thickness of two repeated layer sequences [9, 62]. Holleck et al. [9] classifies multilayers in three main categories:

- Coatings with a limited number of single layers are often used in industry. The layers are thick and to interrupt the columnar growth is their mission.
- The second category covers multilayered coatings with a high number of non isostructural single layers. Beside to interrupt the columnar grain growth, the amount of interfaces

becomes important and consequently the combination of layer material with different characteristics is beneficial.

• Superlattice coatings are the third class. The single bilayer period is in the size of the lattice distance and the interfaces are coherent. Similar chemical bonding, similar atomic ratio and lattice distance are conditions for creating superlattice coatings.

Generally, with decreasing grain size the hardness is improved by hindering dislocation motion, which is the dominant deformation process in materials, by the high number of interfaces according to the Hall Petch relationship [10, 53, 63, 72-74]. This effect is efficient for bilayer periods down to about ten nanometers. Further reduction causes interface sliding as the dominant deformation mechanism. For these bilayer periods the amount of interfaces is very high. Interfaces are weak zones, which are full of voids, allowing a fast diffusion of atoms and vacancies under stress. Further the hardness consequently decreases [10, 11, 63, 75]. In superlattice coatings, hardness is improved by blocking of dislocation motion at the layer interfaces due to the different shear moduli of the layer materials and by the coherency strain causing the lattice mismatch. In this model the dislocation movement is limited by the glide within layers but not across [11, 62, 72]. Hardness and Young's modulus increase with increasing number of layers. In a TiN/ZrN coating with a total film thickness of 4 μm with a number of layers between 100 and 1000, which correspond bilayer periods between 80 and 8 nm, the hardness value is nearly unchanged. The maximum Young's modulus is measured for 50–100 individual layers, with corresponding bilayer periods between 160 and 80 nm. With increasing number of layers the Young's modulus decreases dramatically, which is illustrated in Fig. 9 a). Stueber assumes that the less ductile behavior is caused by micro cracking at the column boundaries [62]. On the other hand Xu et al. [76] reported that the hardness and Young's modulus is nearly constant between 15 and 30 nm bilayer period. In the Ti/TiN multilayer system there is also a critical bilayer period of ~130 nm. A further decrease of the bilayer period causes a massive hardness decrease [77].
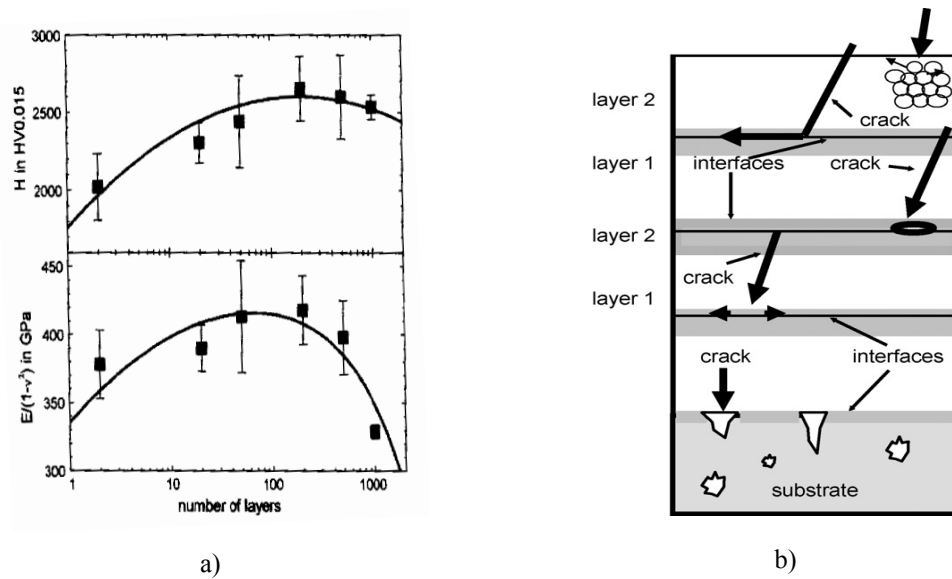
Fig. 9: a) Hardness and Young's modulus of TiN/ZrN multilayer coatings as a function of the number of layers [62], **b)** Schematics of toughening and strengthening mechanisms in ceramic multilayers [9, 62]

Multilayered ceramic coatings have a higher toughness than single layers, because they have a higher interface volume, which absorbs the energy of crack movement [9, 62]. When a crack approaches grain or phase boundaries, it can be split and deflected. This crack energy absorption also works in single layer coatings. In multilayered coatings, the crack movement can also be stopped at the interface zone between the layers, as is shown in Fig. 9 b). On the other side, the toughness can be decreased by local delamination caused by opening of nanovoids, which consequently results in local stress relaxation and even plasticity at the nanoscale [9, 62, 78]. The oxidation resistance can be improved in multilayered materials, where one layer material protects the other layer material against oxidation. Patscheider et al. [8] investigated the nc-TiN/a-Si_3N_4 system. TiN has a limited oxidation resistance at higher temperatures, whereas silicon is known to form hard and stable oxides. Si_3N_4 layers and the oxidized form SiO_2 act as diffusion barrier for oxygen, which prevents oxidation of TiN. With increasing thickness of the Si_3N_4 layer, the oxygen consequently needs more time to reach the TiN phase. TiO_2 has an increased molar volume as compared to TiN, which causes a crack opening of the SiO_x scale. By destroying the diffusion barrier, oxygen reaches TiN more easily and accelerated oxidation of TiN is observed. The multilayered system does not protect TiN against oxidation completely, but nevertheless the oxidation rates are approximately 20 times lower compared to a TiN single layer.

3 Experimental Details

3.1   Coating Deposition

All samples were coated using an Oerlikon Balzers Rapid Coating System (RCS), see Fig. 10 a) [41]. The evaporation ran with six targets, where target 1 & 4 consisted of TiAl, targets 5 & 6 were CrAl and targets 2 & 3 were pure Ti targets. The substrate material was positioned on a rotating carousel stage in the middle of the camber. On the stage were six rotating spindles and one spindle was further divided into six rotating rods. The samples with a hole in the center, e.g. milling inserts, were hanged up on the rods. Tribo discs and mirror-polished SNUN samples were fixed with magnets on the spindle. Samples hanged on the rods had a triple and the tribo discs had a double rotation. This rotation was needed for a homogenous deposition. The geometry of the targets was Ø 160×12mm. Consequently, the targets were not positioned along the whole chamber wall (Fig. 10 b)). Target 2 was located on the lower part of the wall whereas target 3 was located on the upper part.
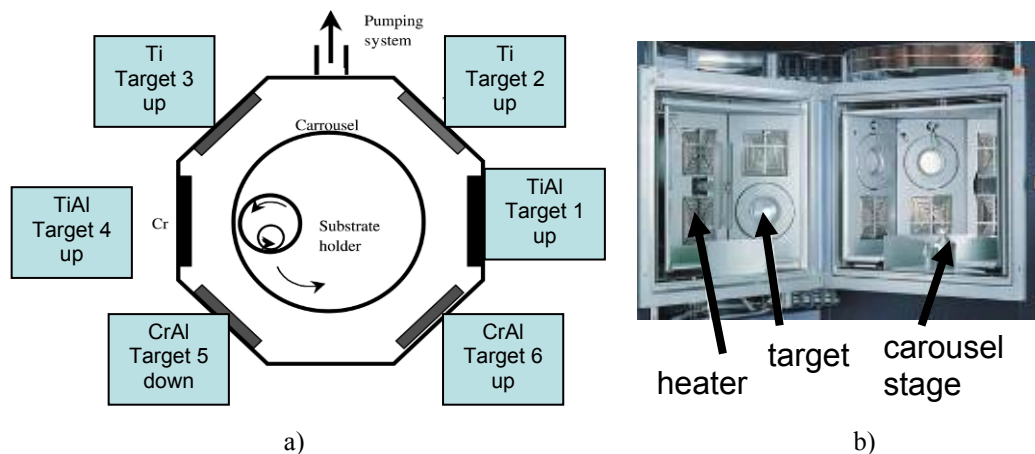

Fig. 10: a) Top view of possible positions of targets and the movement of the samples on the substrate carousel in an Oerlikon Balzers RCS [modified after 41], **b)** chamber of the Oerlikon Balzers RCS [modified after 33]

Before the deposition process was started, all samples were cleaned with ethanol and acetone in an ultrasonic bath. The deposition process needs a temperature of 380 °C for depositing TiN used as adhesion layer between substrate and coating, and 450 °C for the desired coating. The substrate was heated in two ways through inductive heaters and bombardment with ionized argon. The next step was a further cleaning step. The plasma etching is a method where the plasma removes impurities or oxide from the surface. The chamber was backfilled by nitrogen gas as a reactive gas, with a pressure of 8.1×10^{-8} bar. During deposition of TiN only Ti targets, which are in Fig. 10 a) denominated as targets 2 & 3, were used and the rest of the targets were switched off. A negative bias voltage of -150 V was applied between the substrate and the target. For the deposition of the TiAlN/CrAlN multilayer coatings, a bias

voltage of -40 V was used. Both deposition steps ran with a steered arc, where a coil current of 1.4 A was used. During the main deposition the TiAl targets 1 & 4 and the CrAl targets 5 & 6 were used, whereas the Ti targets were switched off. The thickness of the individual layers was controlled by the velocity of the table rotation. On all samples 3 μm thick coatings were grown.

For this thesis 15 deposition runs were performed, called e.g. T50C50-10 where T50 corresponds to the Ti content of targets 1 & 4 and C50 for the Cr content of targets 5 & 6. The last number describes the layer thickness. This nomination is used for all diagrams and explanations in this thesis. For those compositions in Tab. 1, which are signed with "c", the samples are coated with an estimated layer thickness of 300, 100, 30 and 10 nm, respectively. For additional target combinations, signed with "a", only the 10 nm version was deposited. The chemical composition of targets 1 & 4, Ti/Al 50/50, and targets 5 & 6, Ti/Al/Ta 31.7/63.3/5, with layer thickness of 10 nm was used as reference. With this target composition matrix, two coating series were synthesized. In the first series, the target 1 & 4 Ti/Al ratio was kept constant and the Cr/Al ratio of target 5 & 6 changes, i.e. this series is in the following termed constant Ti series. In the second series, the Cr/Al ratio was kept constant and the Ti/Al ratio was changed (constant Cr series). The coatings with target composition T50C50 are the intersection of the two series.

Tab. 1: Matrix of all deposited coatings with different layer thickness and TiAl and CrAl target composition

Target 5/6 / Target 1/4	Al/Cr 70/30	Al/Cr 50/50	Al/Cr 35/65
Ti/Al 33/67		c T33C50-10 T33C50-30 T33C50-100 T33C50-300	Constant Ti series
Ti/Al 40/60		a T40C50-10	
Ti/Al 50/50	c T50C30-10 T50C30-30 T50C30-100 T50C30-300	c T50C50-10 T50C50-30 T50C50-100 T50C50-300	a T50C65-10
Ti/Al 60/40	Constant Cr series	a T60C50-10	

3.2   Coating Characterization

For coating characterization mirror-polished SNUN cutting inserts (ISO-1832, 12.8×12.8×4.8 mm) were used for X-ray diffraction (XRD), transmission electron microscopy (TEM), glow discharge optical emission spectrometry (GDOES), scratch testing

and nanoindentation. For investigation of the surface topography and cross sections by scanning electron microscopy (SEM) SEKW samples in 1204AFSN geometry were used. The determination of the tribological properties was conducted on tribo discs (Ø 30×6 mm) and for cutting tests milling inserts in E-71930-0/1/0 geometry were used. SNUN inserts and tribo discs had the same chemical composition of the substrate, called HM1 in Tab. 2. The SEKW samples and milling inserts had the composition HM2. These were tested against steel as workpiece material.

Tab. 2: Chemical composition of substrate materials

	HM1	HM2
WC [wt.%]	77	87
Co [wt.%]	11	9
Mixed carbides [wt.%]	12	4

For the characterization of the surface and coating morphology, a SEM Zeiss Ultra 55 plus with an acceleration voltage of 20 kV was used. Several samples were investigated by TEM to determine the lattice parameter and the layer thickness. The TEM was a Jeol 2010 FEF with in-column energy filter, working at 200 kV. The chemical composition of the coatings was measured using a GDOES system JY 1000RT from Horiba Jobin-Yvon. The composition was measured during three minutes sputtering time at a pressure of 3×10^{-3} bar and power of 40 W with an anode size of 4 mm. The structural analysis and residual stress of the samples were investigated by XRD using a Bruker D4 Endeavor diffractometer with Cu Kα radiation and a θ-2θ goniometer with parallel beam optics.

The hardness and Young's modulus were measured using a CSM nanoindenter with a Berkovich diamond tip. For the indentation tests a load of 30 mN was used, which resulted in an indentation depth of ~300 nm. To achieve statistically relevant hardness values, 16 indents were averaged. The hardness values were determined using the method of Oliver and Pharr, [79]. To evaluate the scratch resistance and adhesion of the coating, which is determined by the critical load Lc_1, a Revetest Scratch Tester from CSM was used. To achieve statistically relevant Lc_1 values, five scratch tests were made and Lc_1 values were averaged. A Rockwell diamond with a tip radius of 0.05 mm and progressive load from 0 to 15 N, a scratch distance of 10 mm and a speed of 9 mm/min was used. The Lc_1 value was determined optically by a microscope.

For the tribological investigations, a CSM ball-on-disc tribometer was used. The dry sliding experiments were carried out at 25 and 700 °C in ambient atmosphere. The normal load, the sliding speed and the radius of the wear track were kept constant at 5 N, 100 mm/sec and 7 mm, respectively. The frictional partner of all samples was an Al_2O_3 ball with a diameter of 6 mm. The sliding distance was 1000 m at 25 °C and 720 m at 700 °C. After testing the wear tracks were investigated using a Leica DCM3D dual core profilometer in confocal mode using an IX 20 objective. The annealing tests were realized in argon at atmospheric pressure

by a Linn tube furnace. The milling inserts were tested with an EX-CELL-O XB406 machine with a speed of 220 mm/sec without cooling lubricant on 42Cr4Mo steel. For determination of the wear rate of the milling inserts after cutting tests, a FEI Quanta 200 SEM with an acceleration voltage of 20 kV was used.

4 Results

4.1   Chemical Composition

Tab. 3 presents the chemical composition of all multilayered coatings measured by GDOES. In all coatings a nitrogen content of 50 at.% was assumed [40].

Tab. 3: Chemical composition of deposited multilayer coatings

Coating System	Composition [at.%]			
	Ti	Cr	Al	N
Ti/Al 50/50 Ti/Al/Ta 31.7/63.5/5				
T50T31.7-10	18.5	0	30.8	50
Target composition	20.7	0	28.7	50
Ti/Al 50/50 Al/Cr 50/50				
T50C50-10	13.3	15.1	21.6	50
T50C50-30	13.3	15.1	21.6	50
T50C50-100	13	15.9	20.9	50
T50C50-300	12.5	16	21.5	50
Target composition	12.5	12.5	25	50
Ti/Al 50/50 Al/Cr 70/30				
T50C30-10	12.2	12	25.8	50
T50C30-30	11.8	12.2	26	50
T50C30-100	13.9	11.7	24.4	50
T50C30-300	12.7	12.3	25	50
Target composition	12.5	7.5	30	50
Ti/Al 33/67 Al/Cr 50/50				
T33C50-10	9.9	15	25.1	50
T33C50-30	9.9	14.6	25.5	50
T33C50-100	9.7	15.6	24	50
T33C50-300	10	15	25	50
Target composition	8.3	12.5	29	50
Ti/Al 40/60 Al/Cr 50/50				
T40C50-10	11	14.6	24.4	50
Target composition	10	12.5	27.5	50
Ti/Al 60/40 Al/Cr 50/50				
T60C50-10	16	15	19	50
Target composition	15	12.5	22.5	50
Ti/Al 50/50 Al/Cr 35/65				
T50C65-10	12.5	18.5	19	50
Target composition	12.5	16.3	21.2	50

Fig. 11 illustrates a GDOES depth profile of a coating with layer thickness of 30 nm. Caused by surface roughness of the samples and the limited resolution of GDOES, only the averaged Al content of the whole coating can be determined. It is not possible to measure the Al content in the single TiAlN and CrAlN layers separately. Without this knowledge, the lattice parameters of the TiAlN and CrAlN phases and finally the lattice misfit on the interface cannot be determined.
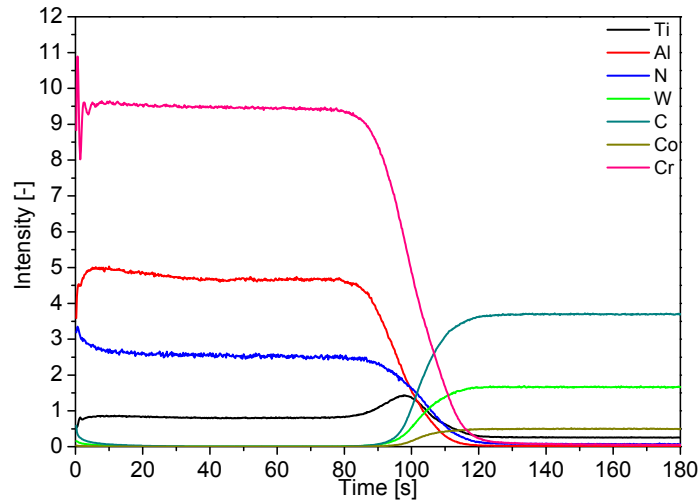
Fig. 11: GDOES depth profile of the coating T33C50-30

Fig. 12 illustrates the Al content of the coating as function of the Al content in the target. The composition of all coatings runs along a line, but the Al content in the target is not exact the same as in the coating. The Al content in the coatings is slightly lower. In contrast, the Ti and Cr content in the coatings is slightly higher as in the targets. The reference coating T50T31.7-10 has a higher Al content because of the 5 at.% Ta in the target, which is not accounted for in Fig. 12. Due to the low weight of Al atoms, more Al gets lost on the way from the target to the substrate due to scattering processes [80].
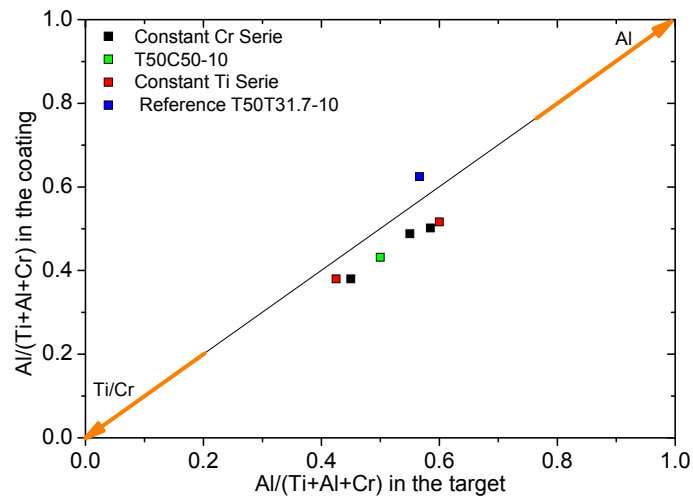

Fig. 12: Average Al fraction of the coating as a function of the Al fraction in the target

According to the target compositions, the deposition runs are divided into a series with constant chemical composition of the Ti/Al target and another series with constant Al/Cr ratio. Fig. 13 combines these two series in one diagram. There, the Al versus the Cr fraction in the constant Ti series and the Al versus Ti ratio in the constant Cr series are illustrated. The Al fraction in the varied layer is linearly fitted and extrapolated to zero for both series. The

sample T50C50-10 is the shared data point in both series. Due to its determination in both series, the constant fraction of Al can be estimated, which can be used to determine the Al content for all chemical compositions of the multilayer.
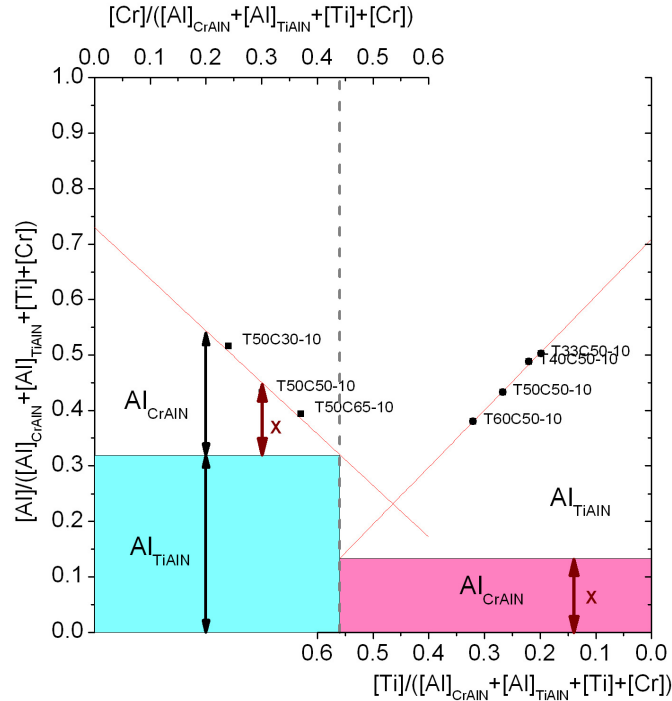

Fig. 13: Al ratio in the coating as function of the variation of Cr and Ti content in the coatings of both series with 10 nm layer thickness

The calculated Al content in the TiAlN and CrAlN layers of the coatings in Fig. 13 are used in Fig. 14 to determine the lattice parameters according to Vegard's law for fcc-AlN and fcc TiN or CrN, respectively [81]. Due to this calculation of the stress free lattice parameter of the different layers, the lattice misfit of the interface between the TiAlN and CrAlN layers can be estimated (cf. Tab. 4). In the constant Ti series, the T50C65-10 sample shows the lowest misfit. It increases with increasing Al content and shows the highest value for T50C30-10. In the constant Cr series the misfit decreases with increasing Al content. The highest value is estimated for T60C50-10 and the lowest one for T33C50-10. These findings correspond well to Vegard's law.
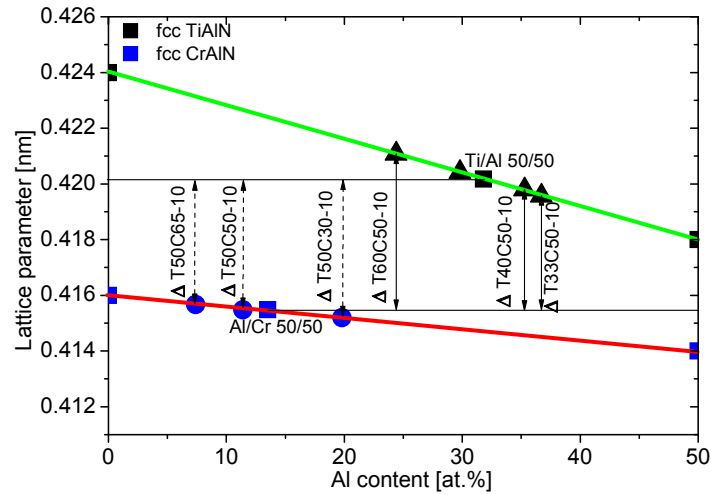
Fig. 14: Lattice parameter of TiAlN and CrAlN layers within the two multilayer coating series with 10 nm layer thickness and determination of the lattice misfit

Tab. 4: Chemical composition of the coatings calculated according to Fig. 13 and lattice parameter calculated according to Fig. 14

	TiAlN		CrAlN				
	Ti [%]	Al_{TiAlN} [%]	Cr [%]	Al_{CrAlN} [%]	Lattice Parameter of TiAlN [nm]	Lattice Parameter of CrAlN [nm]	Misfit [nm]
T50C30-10	27	31.8	21.4	19.8	0.42017	0.4152	0.00497
T50C50-10	27	31.8	29.8	11.4	0.42017	0.41548	0.00469
T50C65-10	27	31.8	33.6	7.4	0.42017	0.41567	0.0045
T33C50-10	10.35	18.35	14.55	6.75	0.41957	0.41549	0.00408
T40C50-10	11.05	17.65	14.55	6.75	0.4198	0.41549	0.00431
T50C50-10	13.8	14.9	14.55	6.75	0.42042	0.41549	0.00493
T60C50-10	16.5	12.2	14.55	6.75	0.42108	0.41549	0.00559

4.2   Surface Topography

The surfaces of all multilayered coatings independent of the chemical composition are rough, see Fig. 15. The roughness is caused by droplets, which are created typically during the arc evaporation process [1]. No significant effect of the coating compositions on the surface topography was evident.
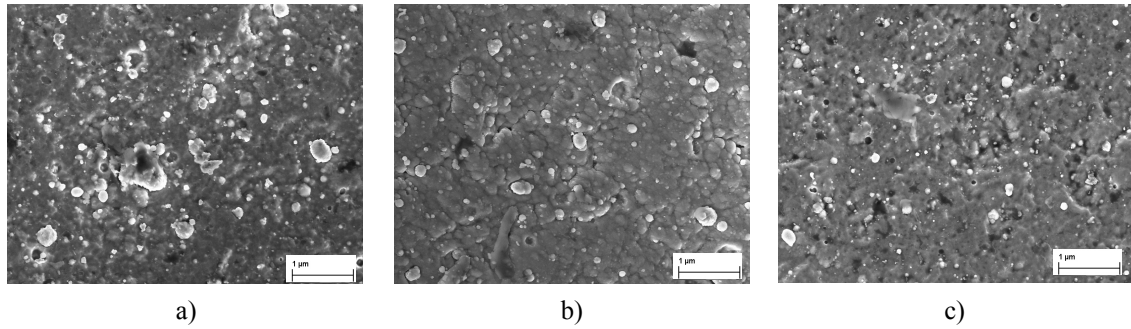

a)   b)   c)

Fig. 15: SEM surface micrographs of coatings deposited with the target compositions **a)** T50C50-100, **b)** T50C30-100, **c)** T33C50-100

The SEM micrographs in Fig. 16 a-d) show the fracture cross-sections of the multilayered coatings with the target composition T50C30 and different layer thickness. The coatings are dense and the grains show a columnar growth over the whole coating thickness. There is no obvious change of the structure for the different layer compositions. Coatings with a layer thickness of 10 and 30 nm are too thin to distinguish between the individual layers by SEM. For coatings with a layer thickness of 100 and 300 nm, respectively, the layers are clearly visible. The TiAlN layer has the same thickness as the CrAlN layer, as shown in Fig. 16 c, d).
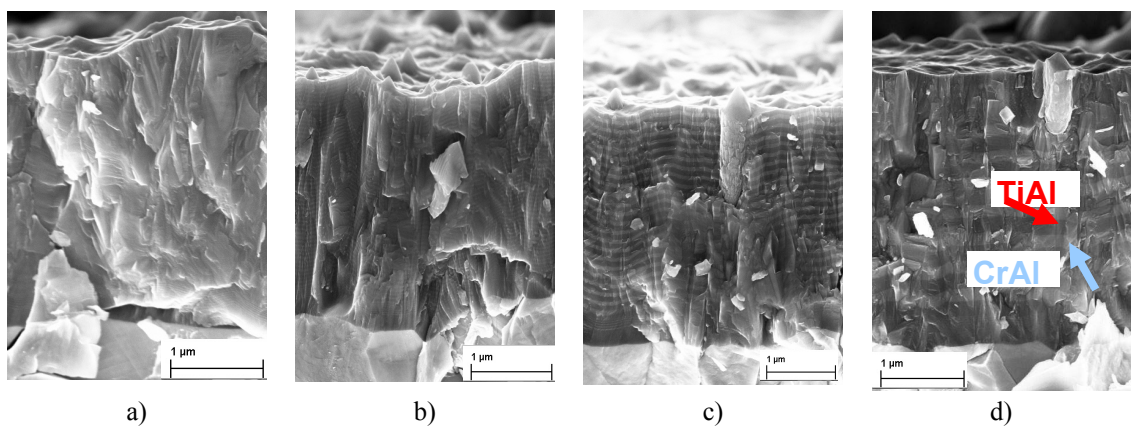

a)   b)   c)   d)

Fig. 16: SEM fracture cross-sections of multilayered coatings with target composition T50C30 and different layer thickness **a)** 10 nm, **b)** 30 nm, **c)** 100 nm, **d)** 300 nm. The dark layer is TiAlN, the bright one CrAlN

The SEM images in Fig. 17 illustrate the fracture cross-sections of an Al rich CrAlN layer and an Al rich TiAlN layer in Fig. 17. The coatings are characterized by a comparable grain structure independent of which layer is Al rich.
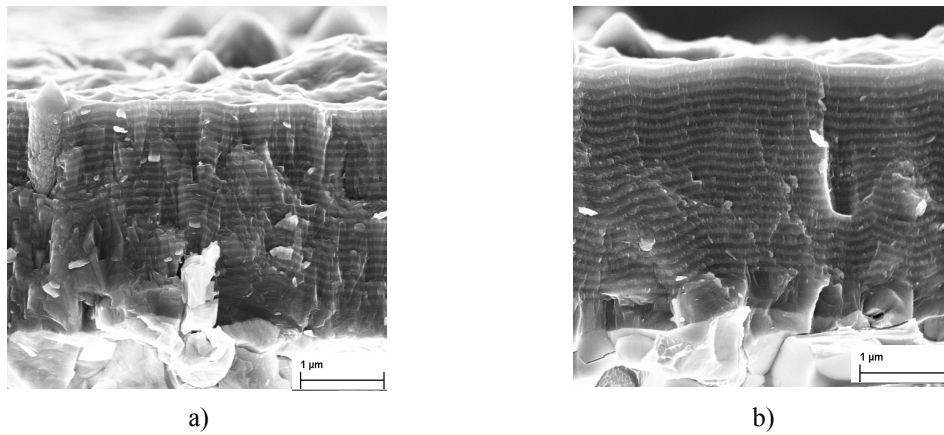
<center>a)   b)</center>

Fig. 17: SEM fracture cross-sections of **a)** T50C30-100, **b)** T33C50-100

4.3   Coating Structure

In this section the results obtained on the coating microstructure are presented. In Fig. 18 a-c) representative XRD patterns of the coatings T33C50-10, T50C50-10 and T50C30-10 are illustrated. According to the multilayered architecture, the XRD patterns of the TiAlN and CrAlN phases overlap. Independent of the Al content in the coatings, no evidence of hcp phases was found; all peaks belong to the fcc phases.
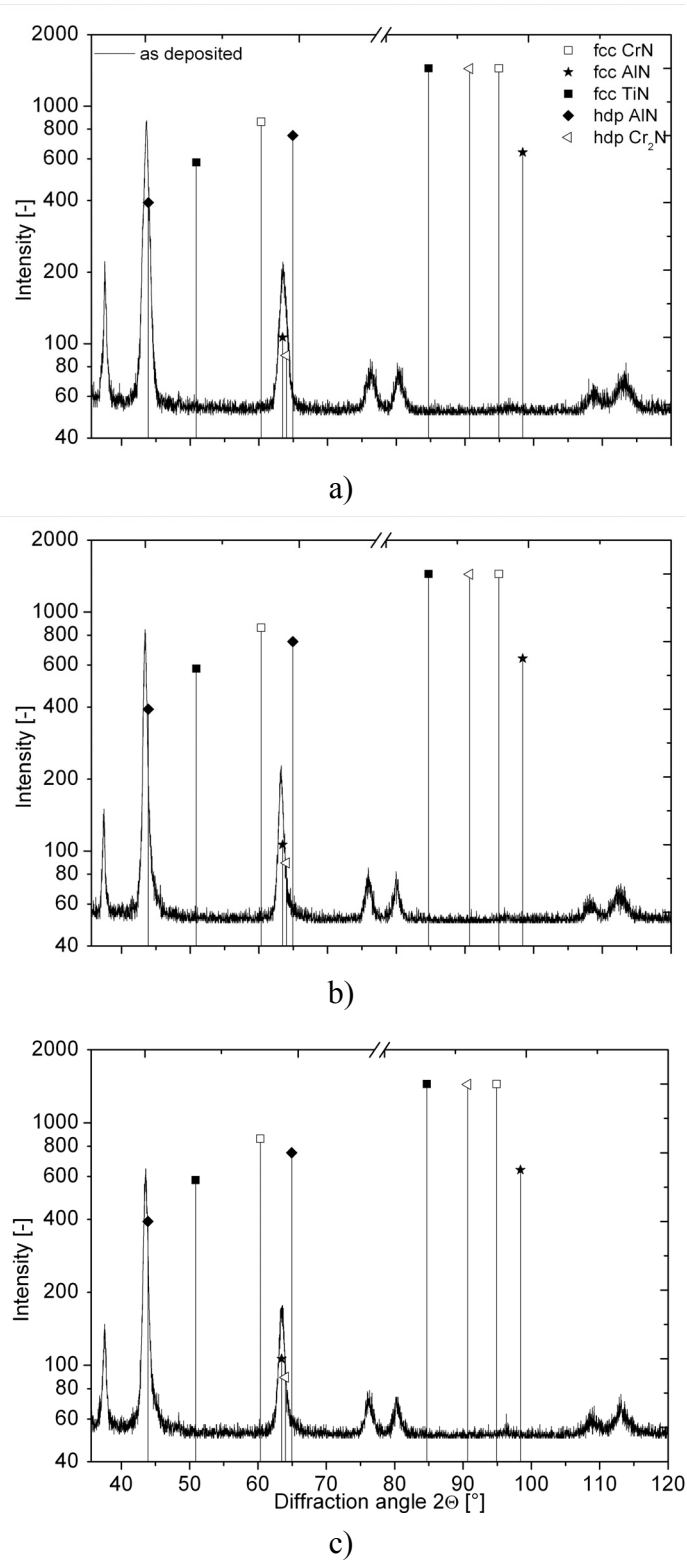
Fig. 18: XRD patterns of coatings **a)** T50C30-10, **b)** T50C50-10, **c)** T33C50-10

4.3.1 Full width at half maximum (FWHM)

The full width at half maximum is determined from the XRD patterns and gives an estimation of the size of the crystallites. It has to be taken into account that due to the overlapping peaks of TiAlN and CrAlN only an average value for both layers can be obtained. With increasing

Al content the peak width of the constant Ti series decreases slightly from 9.4 to 7.4 nm whereas the peak width of the constant Cr series increases from 8.0 to 8.9 nm (Fig. 19 a, b)). The reference however showed a slightly higher FWHM value, Fig. 19 a). The peak width also depends on the layer thickness, see Fig. 19 c). Coatings with a layer thickness of 10 nm have high FWHM values between 7.4 and 8.4 nm. These decrease with increasing layer thickness. Samples with the target compositions T50C50 and T33C50 have the lowest peak width of 4.9 and 5.8 nm at 100 nm layer thickness, whereas sample T50C30 has the lowest value 5.6 nm at 30 nm. Between 100 and 300 nm layer thickness for all target compositions, the peak width increases again. Samples with high Al content in the target reach values comparable to the 10 nm layer thickness, whereas the sample with T50C50 target composition only shows a slightly increase.
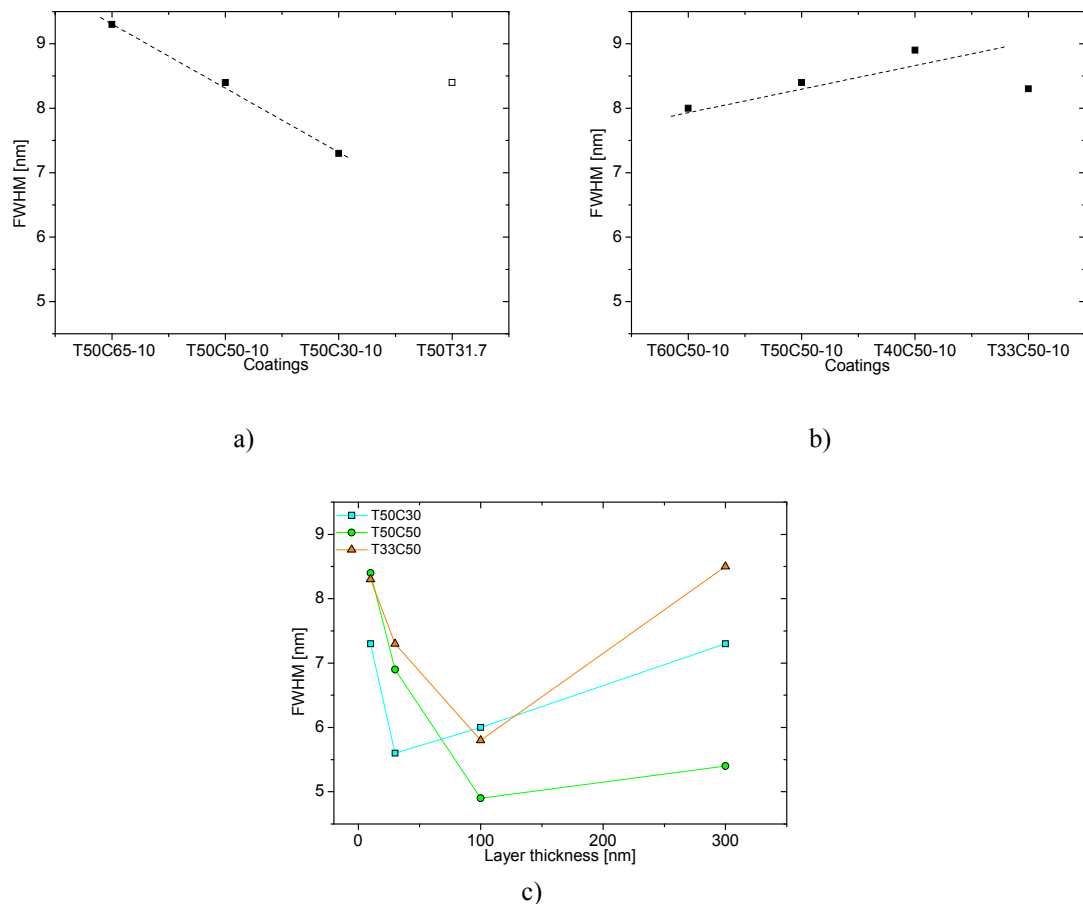

a)   b)

c)

Fig. 19: Full width at half maximum **a)** constant Ti series, **b)** constant Cr series, **c)** effect of the layer thickness

4.3.2 Residual Stress

The residual stress is determined by the peak shift of the XRD patterns. All investigated multilayered coatings show compressive stresses. In the constant Ti series, shown in Fig. 20 a), the normal stress value is around -2300 MPa and nearly constant with varying Al content. Fig. 20 b) illustrates the normal stress of the constant Cr series, which increases with

increasing Al content, where the lowest value is measured at -1160 MPa at a target composition T60C50 and the highest value to -3010 MPa at T33C50. The residual stress is nearly independent of the layer thickness, see Fig. 20 c). Samples of the target with composition T33C50 show the highest residual stress values around -3300 MPa, whereas samples with composition T50C30 have the smallest values with -2300 MPa. The samples with T50C50 composition are characterized by residual stress values around -2500 MPa and the values are between both Al-rich coatings.
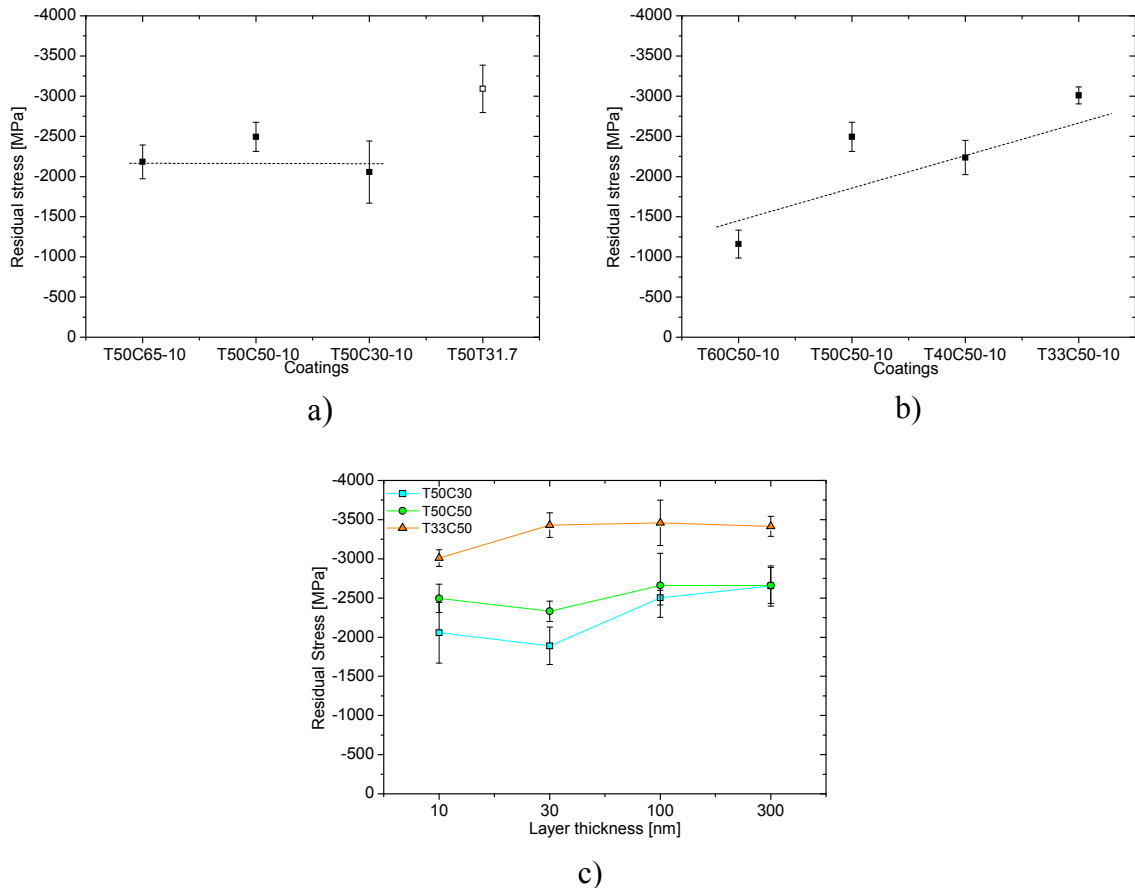

Fig. 20: Residual stress a) constant Ti series, b) constant Cr series, c) effect of the layer thickness

4.3.3 Transmission Electron Microscopy

T50C50-10, T50C65-10, T33C50-10 and T60C50-10 samples were characterized by TEM to determine the actual layer thickness. All coatings independent of the chemical composition showed similar layer thicknesses between 10 and 13.5 nm. In Fig. 21 a representative TEM bright field micrograph of sample T33C50-10 is shown. The TEM micrographs of all other coatings are illustrated in the appendix.
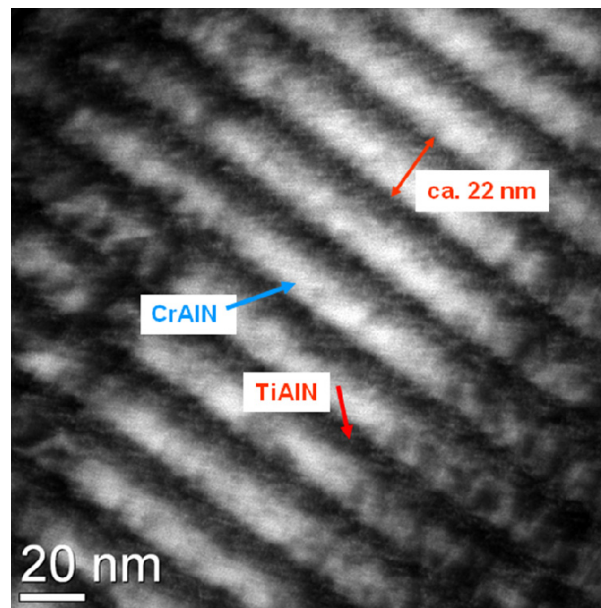
Fig. 21: TEM bright field image of the layer architecture of the coating T33C50-10

For the sample T33C50-10 the lattice parameter was determined from high resolution micrographs by selected area electron diffraction (SAED), see Fig. 22. The TiAlN single layer had a lattice parameter of 0.4090 nm, as measured in dark area, labeled "a" in Fig. 22. In the bright area, labeled "b", the lattice parameter of the CrAlN layer was determined to 0.4070 nm.
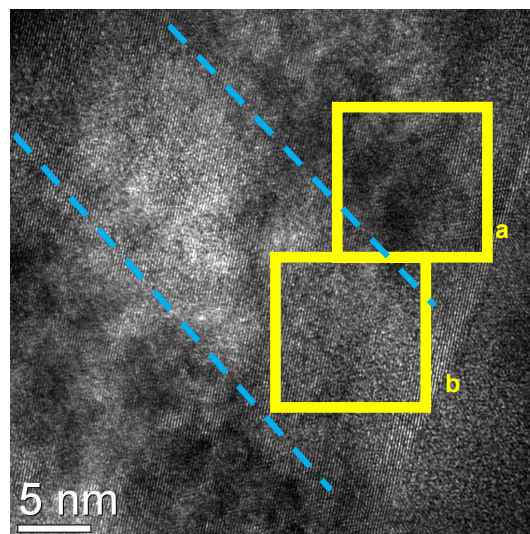

Fig. 22: High resolution micrograph of single layers of the coating T33C50-10

4.4   Hardness and Young's Modulus

The coating hardness in the constant Ti series reached a value of ~28.5 GPa, independent of the Al content, see Fig. 23 a). In contrast, the constant Cr series, as shown in Fig. 23 b), an increasing hardness with increasing Al content in the coating was measured. In both series the Young's modulus showed comparable values of ~450 GPa, independent of the Al content.

The highest hardness and Young's modulus values in both series were measured for the reference coating T50T31.7-10.

Fig. 23 c) illustrates the hardness and the Young's modulus depending on the layer thickness. The target composition T50C50 resulted in a hardness of around 29 GPa and Young's modulus of 500 GPa. The hardness of the coatings T50C30 showed for the layer thickness between 10 and 100 nm a value of ~28 GPa, which increased to ~32 GPa for the layer thickness of 300 nm. There the Young's modulus is constant at ~500 GPa and independent of the layer thickness. Between 10 and 30 nm layer thickness, the hardness of coatings with the target composition T33C50 increased slightly from 29.5 to 30.2 GPa and decreased for the 100 nm layer thickness to 26 GPa. For 300 nm layer thickness, the hardness yielded the value 30.3 GPa. In contrast, the Young's modulus decreased with layer thickness increasing from 10 to 100 nm from ~460 to ~380 GPa. Similar to the hardness, the Young's modulus increased again to ~430 GPa at a layer thickness of 300 nm.
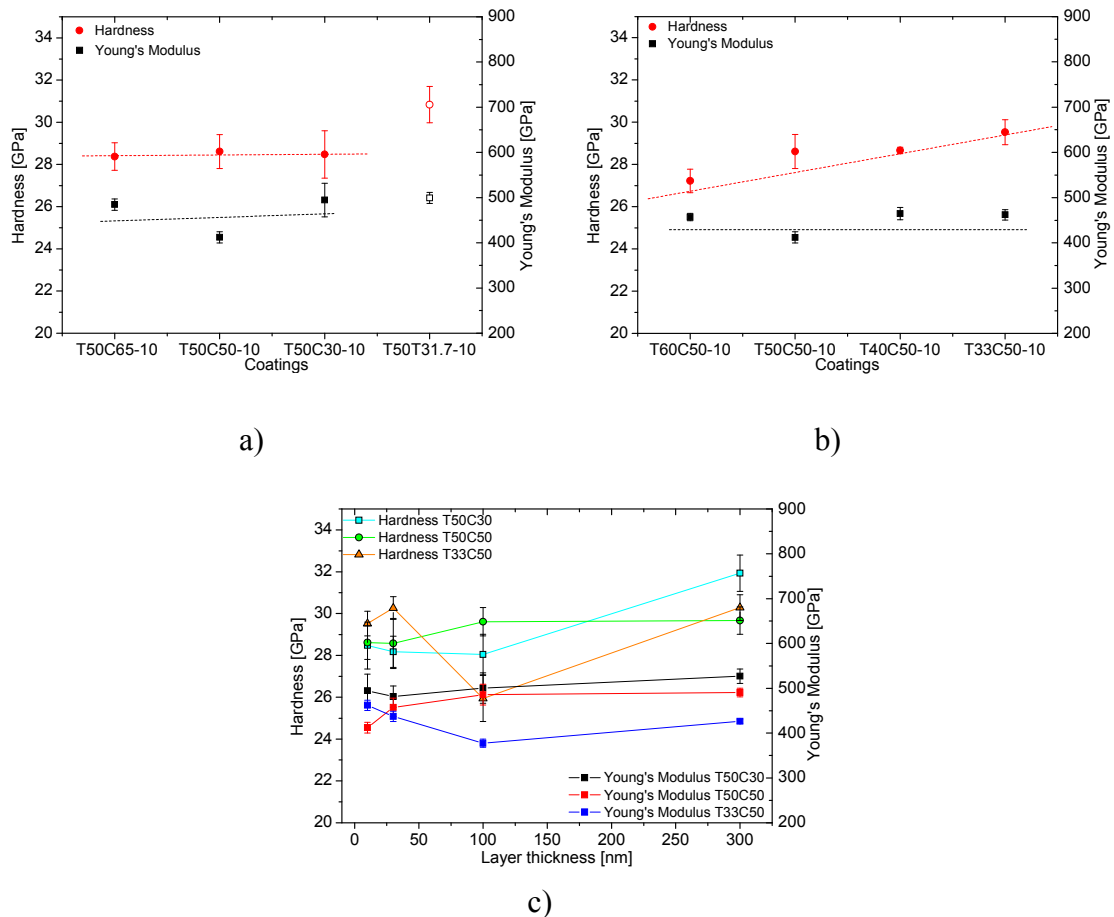

a)   b)

c)

Fig. 23: Hardness and Young's modulus **a)** constant Ti series, **b)** constant Cr series, **c)** effect of layer thickness

4.5   Coating Adhesion

Fig. 24 a) illustrates the critical load Lc_1 of the coatings of the constant Ti series with 10 nm layer thickness with increasing Al content of the samples. The sample T50C65-10 with the lowest Al content of this series had the highest Lc_1 of 13.2 N. With the addition of 2.1 at.% Al, the Lc_1 value decreased to 12.3 N. The lowest Lc_1 of 10.5 N was measured for coating T50C30-10. For comparison, the reference T50T31.7-10 showed the highest Lc_1 value of 15.4 N. The scratch tracks are summarized in Fig. 24 b-e). The delamination at the scratch border zone of the tracks is caused by overloading with higher values than Lc_1, which indicates poor adhesion of the coating.
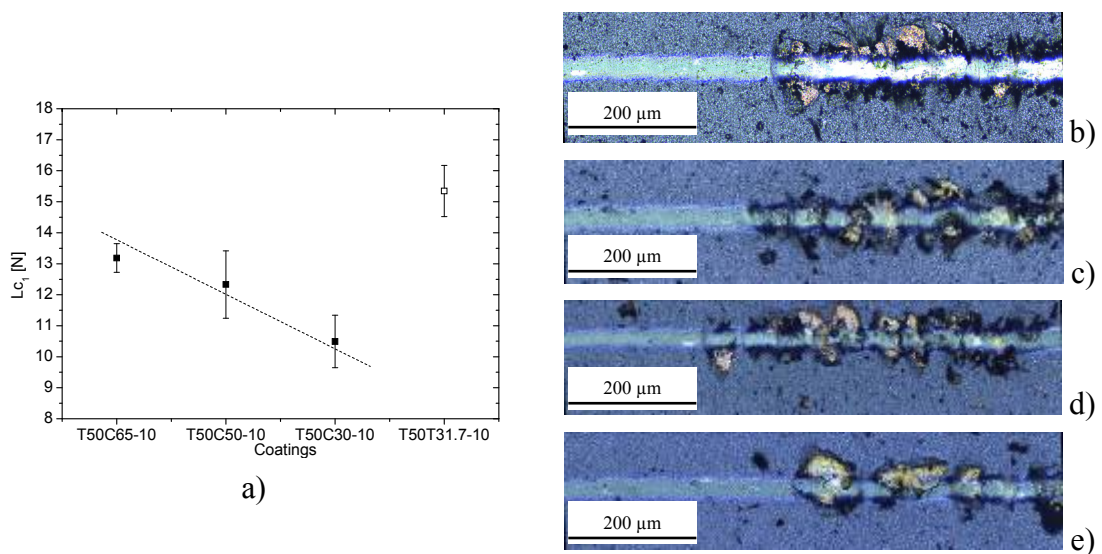

Fig. 24: a) Critical load Lc_1 as function of increasing Al content. Scratch tracks of coatings **b)** T50C65-10, **c)** T50C50-10, **d)** T50C30-10, **e)** T50T31.7-10

The Lc_1 value of the constant Cr series as function of the Al content is shown in Fig. 25 a). With the Al content in the coating increasing from 19 to 21.6 at.%, Lc_1 increased from 11.3 to 12.3 N. At higher Al content the Lc_1 values decreased and the minimum Lc_1 value of 10 N was measured for coating T33C50-10. All samples showed delamination at the border of the scratch track above Lc_1, see Fig. 25 b-d).
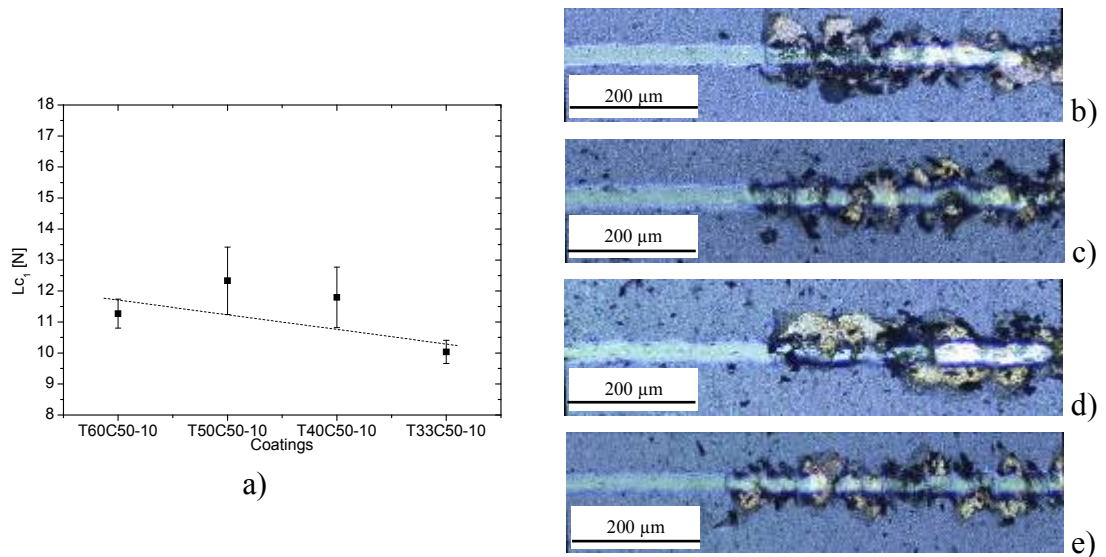
Fig. 25: a) Critical load Lc_1 as function of increasing Al content. Scratch tracks of coatings **b)** T60C50-10, **c)** T50C50, **d)** T40C50, **e)** T33C50

Fig. 26 illustrates the Lc_1 values as function of the layer thickness of samples of three different target compositions. The samples coated with target ratios Ti/Al 33/67 and Cr/Al 50/50 showed an increased Lc_1 with increasing layer thickness. The lowest Lc_1 value of 10 N was measured for the layer thickness of 10 nm and the highest with 16.2 N for a thickness of 300 nm. Samples with the target composition Ti/Al 50/50 and Cr/Al 50/50 showed for the layer thickness between 10 and 30 nm constant Lc_1 values of 12.3 to 12.5 N, whereas the value decreased to 9.9 N for a layer thickness of 300 nm. The Lc_1 values of the samples of the targets Ti/Al 50/50 and Cr/Al 30/70 decreased from 10 to 30 nm layer thickness by only 0.2 N. In contrast, the highest Lc_1 value of 15.5 N was determined for a layer thickness of 100 nm. At a layer thickness of 300 nm, the value decreased slightly to 15.1 N.
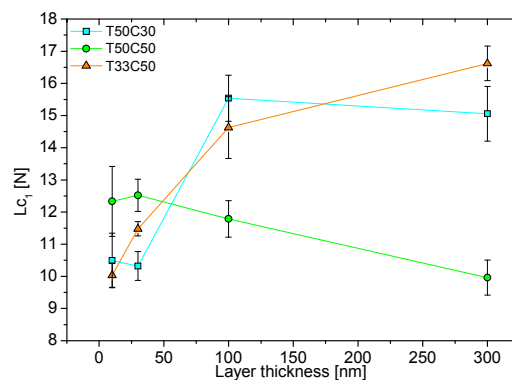

Fig. 26: Critical load L_1 as function of layer thickness for coatings with different target compositions

4.6   Tribological properties

The coefficient of friction (CoF) and the coefficient of wear (CoW) depending on the sliding distance at room temperature and 700 °C are illustrated in Fig. 27 a, b). With increasing chromium content, both CoF and CoW decrease significantly at room temperature. For T50C65-10 with the highest chromium content in the coating, the lowest CoF and CoW with values of 0.3 and ~1.67×10^{-16} m^3/Nm, respectively were determined. Compared to the reference T50T31.7-10, which does not have any chromium, the highest CoF (0.9) and CoW (3.8×10^{-5} m^3/Nm) were measured (cf. Fig. 27 a). In contrast, the constant Cr series showed similar values for CoF and CoW of ~0.6 and ~3.5×10^{-16} m^3/Nm at room temperature, with the exception of T33-50-10 which showed an increased CoW of 1.05×10^{-15} m^3/Nm.

At 700 °C all samples showed similar CoF of ~0.7, with exception of the reference with a CoF of 0.88. The CoW of the constant Ti series, including the reference, showed a value of ~9×10^{-16} m^3/Nm. For the coating T50C50-10, a significantly lower value of 2.7×10^{-16} m^3/Nm was determined. For the constant Cr series, a CoW of ~3.5×10^{-16} m^3/Nm was measured independent of the Al content. An exception is coating T33C50-10 which showed an increased CoW of 9.7×10^{-16} m^3/Nm.
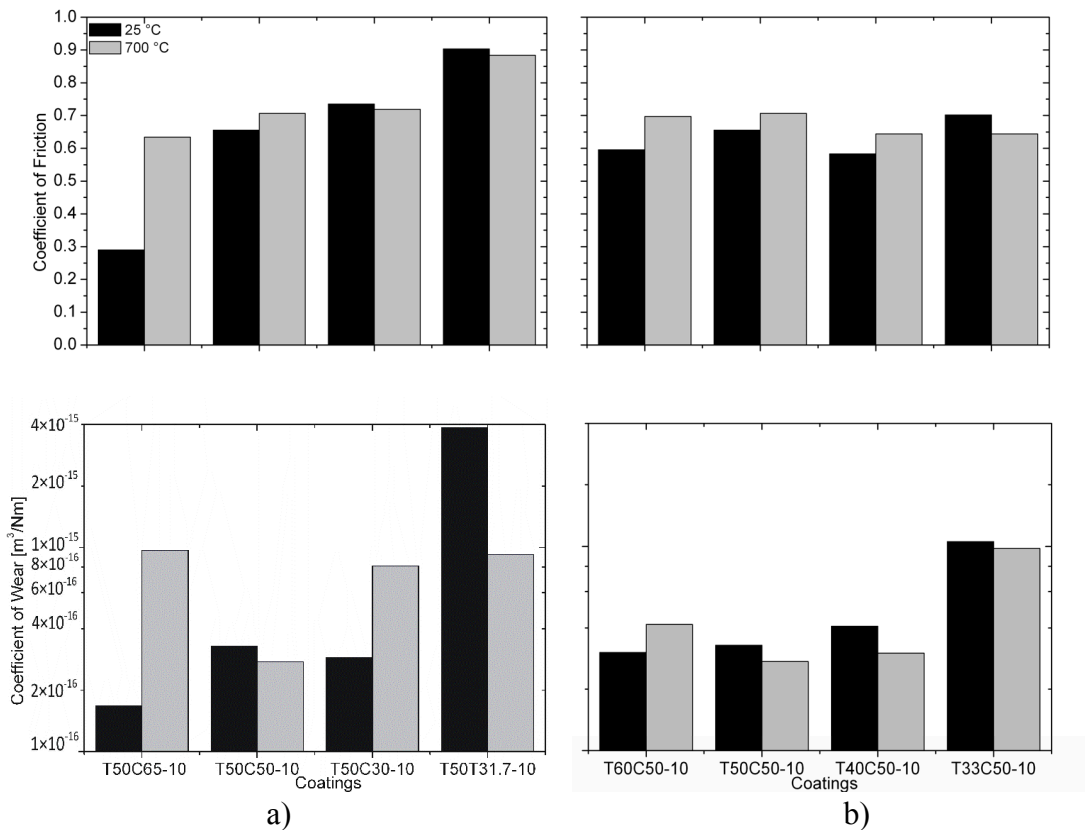

Fig. 27: Coefficient of friction and coefficient of wear at room temperature and at 700 °C of a) constant Ti series, b) constant Cr series

Fig. 28 illustrates the CoF and the CoW at room temperature and at 700 °C as function of the layer thickness. At room temperature the Al rich samples T50C30 and T33C50 showed similar CoF values. With increasing layer thickness, they tend to decrease. The highest value of ~0.71 was measured at 10 nm and the lowest value ~0.55 is determined for 300 nm layer thickness. The samples of T50C50 with layer thickness of 10 and 30 nm showed similar CoF with values of ~0.65. With layer thickness increasing to 100 nm, the CoF decreased to 0.5 and with a further increase the CoF increases to 0.71. Similar and constant CoW values between 3×10^{-16} and 4.5×10^{-16} m^3/Nm were determined for the samples with 10 to 100 nm layer thickness of the target compositions T50C50 and T50C30. With layer thickness increasing to 300 nm, the CoW value of T50C50 increased significantly to 1.1×10^{-15} m^3/Nm, whereas the value of T50C30 was nearly constant at 4.2×10^{-16} m^3/Nm. The CoW of T33C50 decreased significantly with increasing layer thickness. The coating T33C50-10 showed the highest value of 1.0×10^{-15} m^3/Nm, and the lowest value of 1.5×10^{-16} m^3/Nm was determined for a layer thickness of 300 nm. At 700 °C all coatings, independent of the composition and layer thickness, showed a similar CoF of ~0.7. An exception is T50C50-300, which showed an increased CoF value of 0.81. The CoW of T33C50 was nearly constant at 8×10^{-16} m^3/Nm independent of the layer thickness. The CoW values of coatings of target composition T50C30 decreased significantly from 8.1×10^{-16} for 10 nm layer thickness to 1.4×10^{-16} m^3/Nm for 100 nm. With increased layer thickness, the CoW increased further to 5.4×10^{-16} m^3/Nm. T50C50-10 showed a low CoW of 2.7×10^{-16} m^3/Nm. With layer thickness increasing to 30 nm, the value increased significantly to 1.3×10^{-15} m^3/Nm. With further increase of the layer thickness, the CoW decreased significantly again to 1.5×10^{-16} m^3/Nm. The coating with 300 nm layer thickness showed a significantly increased CoW value of 8×10^{-16} m^3/Nm again.

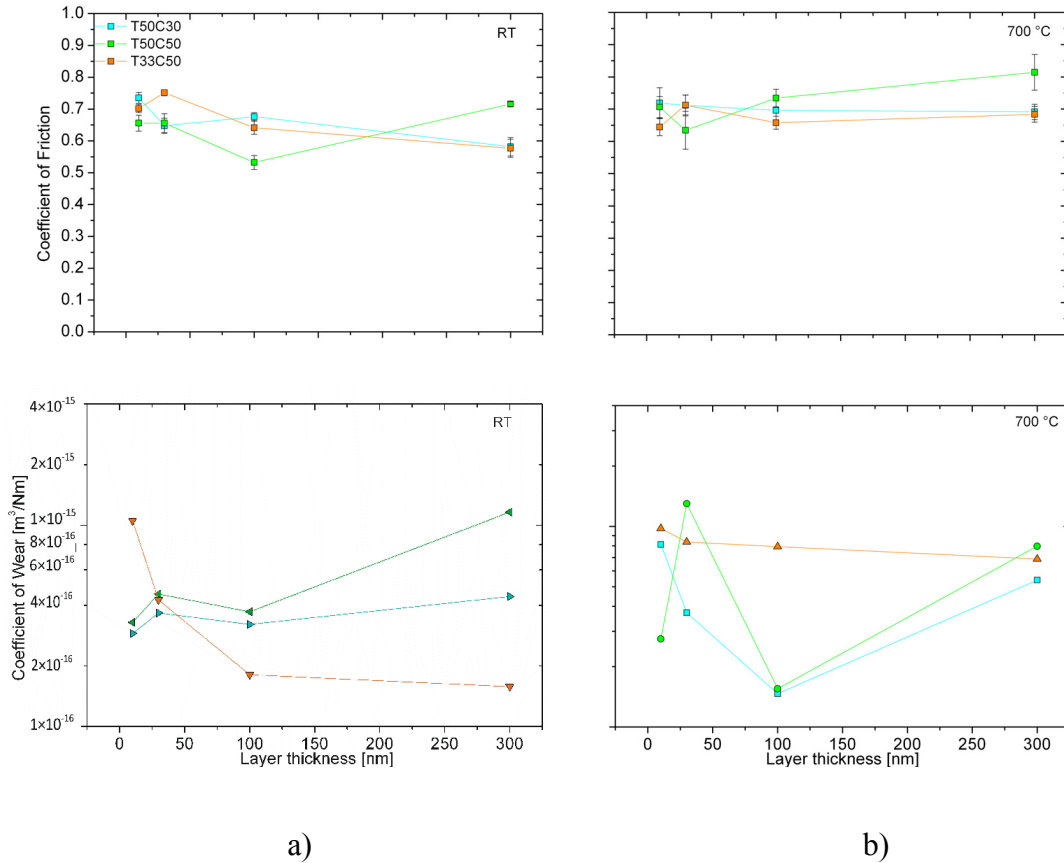<p style="text-align:center;">a)   b)</p>

Fig. 28: Coefficient of friction and coefficient of wear as function of the layer thickness at **a)** room temperature, **b)** 700 °C

4.7 Thermal stability

To determine the hardness and the crystallographic structure of the coatings after heat treatment, annealing tests for the samples with 10 nm layer thickness were conducted. Five runs were realized with annealing temperatures at 600, 700, 800, 900, 1000 °C and two hours annealing duration in Ar atmosphere. Additional six annealing runs were conducted at 700, 800 and 900 °C with durations of 4 and 8 hours (Tab. 5.).

Tab. 5: Summary of annealing temperatures and durations of the heat treatments

Annealing Temperature [°C]	600	700	800	900	1000
Annealing Duration [h]	2	2, 4, 8	2, 4, 8	2, 4, 8	2

4.7.1 Microstructural changes

Fig. 29 a-c) shows the XRD patterns of coatings within the constant Ti series for increasing Al content in the as-deposited state and after annealing at 800, 900 and 1000 °C for two hours. The patterns of the samples annealed at 600 and 700 °C are illustrated in the appendix because of the similarity to those determined at room temperature. In Fig. 29 d) all XRD patterns of the constant Ti series at 1000 °C are summarized. For all XRD measurements, the

significant peaks are illustrated in the 2θ region from 35° to 46°. The position of the dominant peak is found at 2θ ~43° for all temperatures, which corresponds to the (100) crystallographic orientation of the fcc phase. At the diffraction angle of ~37° another major peak appears, which corresponds to the (111) crystallographic orientation. Because of the multilayered structure, the XRD patterns overlap for the TiAlN and CrAlN peaks, and the position of the peaks is also slightly shifted. With increasing Al content, the dominant peaks shift by $\Delta 2\theta$ ~0.7° to higher diffraction angles in the as-deposited state. After annealing at 800 °C, both peaks of all coatings are slightly shifted to higher 2θ angles. After annealing above 800 °C, the samples showed different XRD patterns. Fig. 29 a) illustrates the XRD pattern for coating T50C65-10. The position of the main peaks shifted back to lower diffraction angles after annealing at 900 and 1000 °C. Annealing of sample T50C50-10 at 800 °C showed an increased peak width of the dominant peaks, and after annealing at 1000 °C the peak at 2θ ~43° separates into a double peak (Fig. 29 b)). For this sample, the peak at 2θ ~37° is shifted to lower angles after annealing at 1000 °C. The coating T50C30-10 showed a similar behavior as coating T50C65-10, but in contrast it tends to create a more pronounced double peak already at 900 °C, see Fig. 29 c). T50C30-10 also showed an hcp AlN phase at 1000 °C. The peak is positioned at 2θ ~36° and has an (001) crystallographic orientation. In summary, there seems to be a higher driving force for decomposition in Al rich multilayer, see e.g. the peaks at 2θ ~43° for coatings T50C65-10 and T50C30-10 in Fig. 29 d). The reference coating T50T31.7-10 has the dominant position close to the peak position of TiAlN due to the absence of Cr.
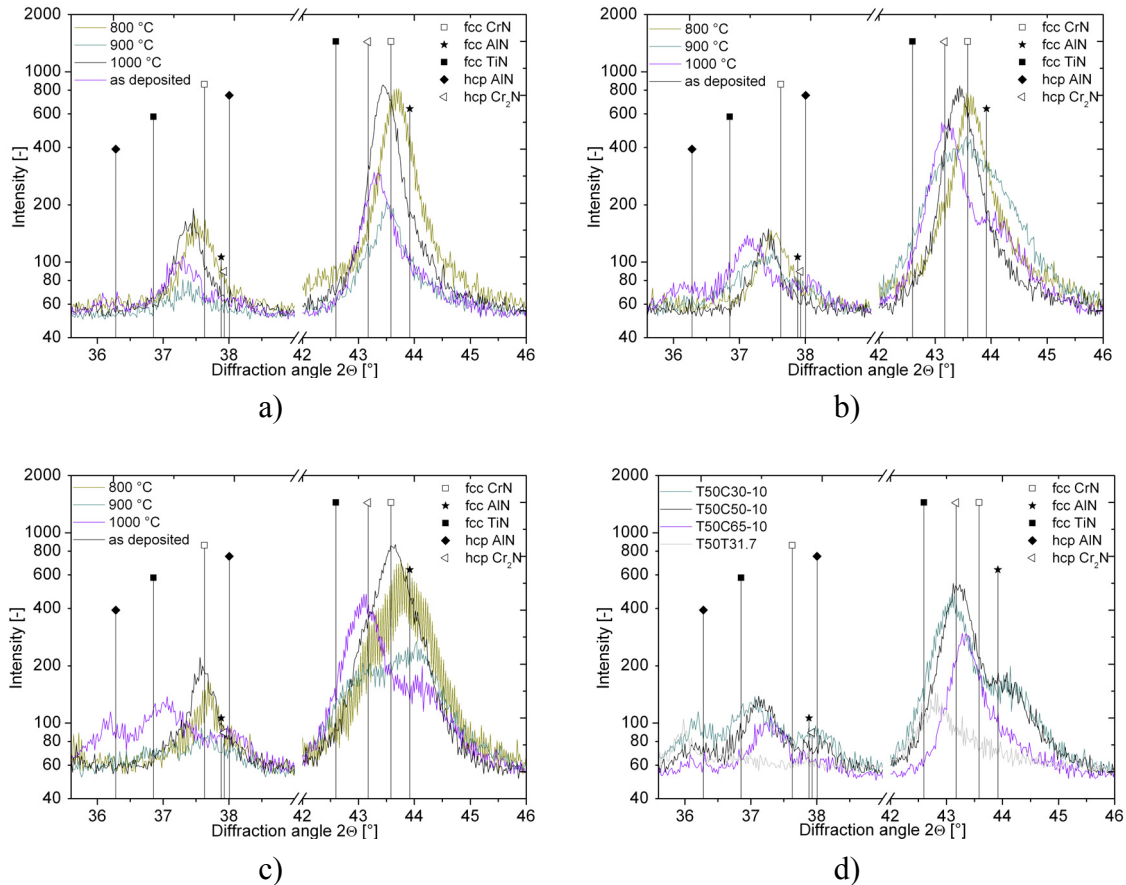
Fig. 29: XRD patterns of coatings **a)** T50C65-10, **b)** T50C50-10, **c)** T50C30-10, annealed at 800, 900, 1000 °C for 2 h compared to the as-deposited state, and **d)** comparison of T50C65-10, T50C50-10, T50C30-10 and T50T31.7-10 annealed at 1000 °C for 2 h

The XRD pattern of the constant Cr series is also shown in the appendix because of the similar behavior as the constant Ti series.

Fig. 30 a-c) summarizes the results obtained for the constant Ti series after annealing at 900 °C with different durations, including the XRD pattern for the as-deposited state. After annealing, the peaks of coating T50C65-10 showed similar positions as in the as-deposited state, independent of the annealing duration (Fig. 30 a)). After 2 hours annealing, the peak width was similar as in the as-deposited state, in contrast to annealing for 4 and 8 hours, where the peak width increased. Also the hcp AlN phase was formed after annealing for 4 and 8 hours. The XRD patterns of sample T50C50-10 also showed peak broadening similar to the coating T50C65-10, but in contrast the process already starts after 2 hours annealing and is more significant, see Fig. 30 b). Because of the increased Al content in the coating, the hcp AlN peak appeared at a diffraction angle 2θ of ~36°. The coating T50C30-10 showed a different XRD pattern compared to samples T50C65-10 and T50C50-10, illustrated in Fig. 30 c). With increasing annealing duration, the dominant peaks are separated into a double peak. The formed hcp AlN peak is also more pronounced compared to T50C50-10.
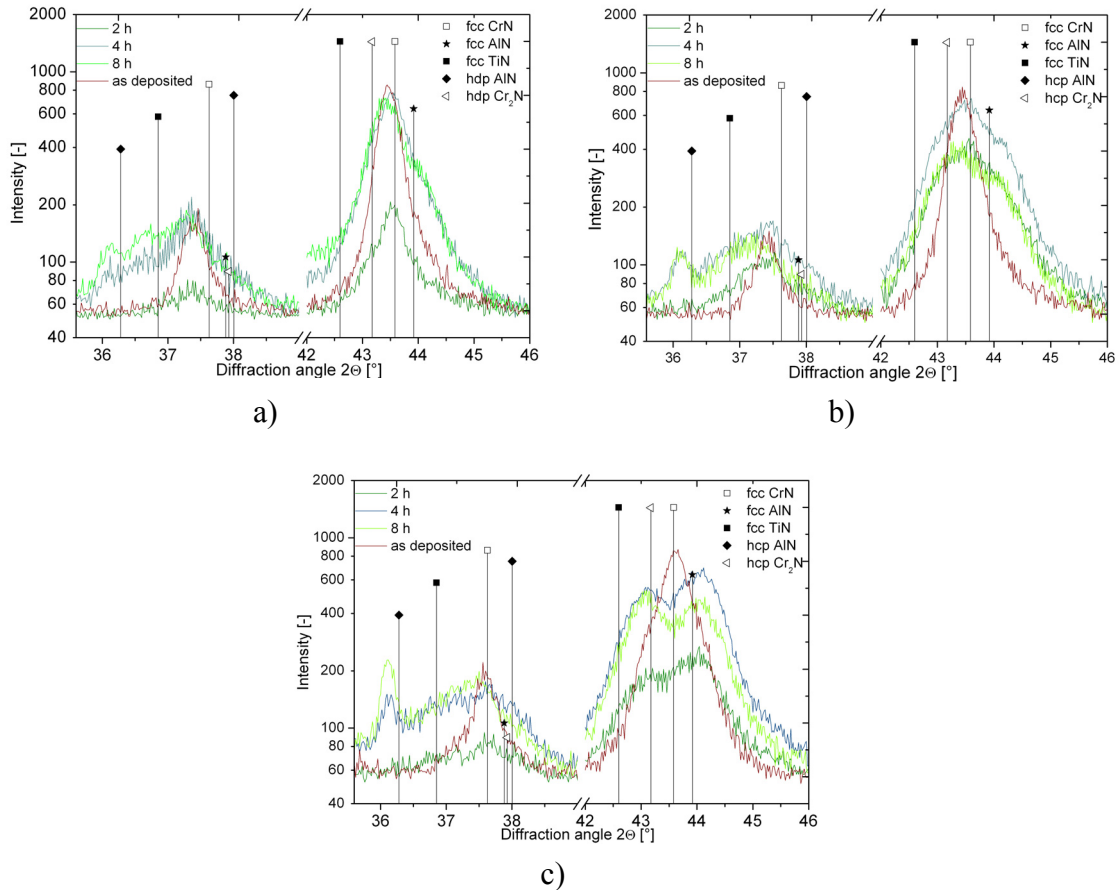
Fig. 30: XRD patterns of coatings **a)** T50C65-10, **b)** T50C50-10, **c)** T50C30-10, annealed at 900 °C with annealing duration of 2, 4 and 8 h and compared to the as-deposited state

For all XRD patterns, no Cr_2N peaks could be determined, independent of the annealing temperature and duration.

4.7.2 Hardness

The hardness of all coatings with 10 nm layer thickness after annealing for 2 hours as function of different annealing temperatures is shown in Fig. 31. In the as-deposited state, sample T33C50-10 with high Al content showed the highest hardness value of 29.5 GPa. The lowest value of 27.2 GPa was measured for coating T60C50-10. The other coatings had a similar hardness of ~28.6 GPa. Independent of the annealing temperature, samples T33C50-10 and T50C30-10 showed the highest hardness of all samples. In particular, the highest hardness with 34.5 GPa was determined for coating T50C30-10 after annealing at 600 °C. In contrast, samples T50C65-10 and T60C50-10 with low Al content showed the lowest hardness values above 700 °C. After annealing at 1000 °C, the hardness of all coatings decreased significantly and only hardness values below 24.5 GPa were determined, see Fig. 31.
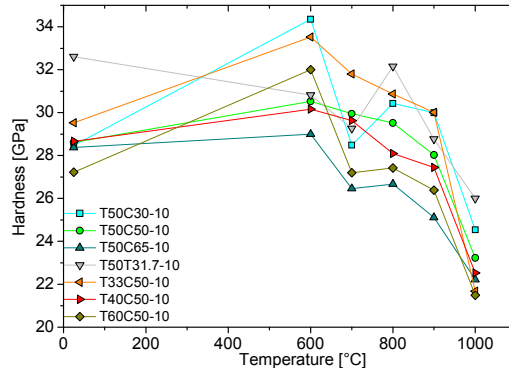
Fig. 31: Hardness of multilayer coatings with 10 nm layer thickness, annealed for 2 h with varying temperature

In Fig. 32 a-c) the hardness of coatings within the constant Ti series after annealing at 700, 800 and 900 °C for different durations is plotted. Independent of the annealing temperature and duration, the coating T50C65-10 showed the lowest hardness, and was even below the room temperature value. After annealing at 700 °C with different durations, the coatings T50C65-10 and T50C50-10 showed higher hardness values compared to the hardness after annealing at 800 and 900 °C. In contrast, the coating T50C30-10 showed higher hardness values after annealing at 800 °C. After 4 hours annealing, T50C30-10 yielded a maximum hardness of 31.1 GPa, which is the highest value obtained within the constant Ti series.

After annealing at 800 °C, coatings T50C65-10 and T50C50-10 showed a similar tendency of decreasing hardness values with increasing annealing duration. For annealing at 900 °C, the hardness of coatings T50C50-10 and T50C30-10 decreased slightly with increasing annealing duration. However, the coating T50C30-10 showed a higher hardness value after 2 hours annealing than at room temperature. After annealing for 2 hours at 900 °C, the hardness of coating T50C65-10 decreased similar as the coating T50C50-10. In contrast, after 4 hours annealing at 900 °C the hardness of coating T50C65-10 increased again to a value of 27.4 GPa and remained constant after 8 hours annealing.
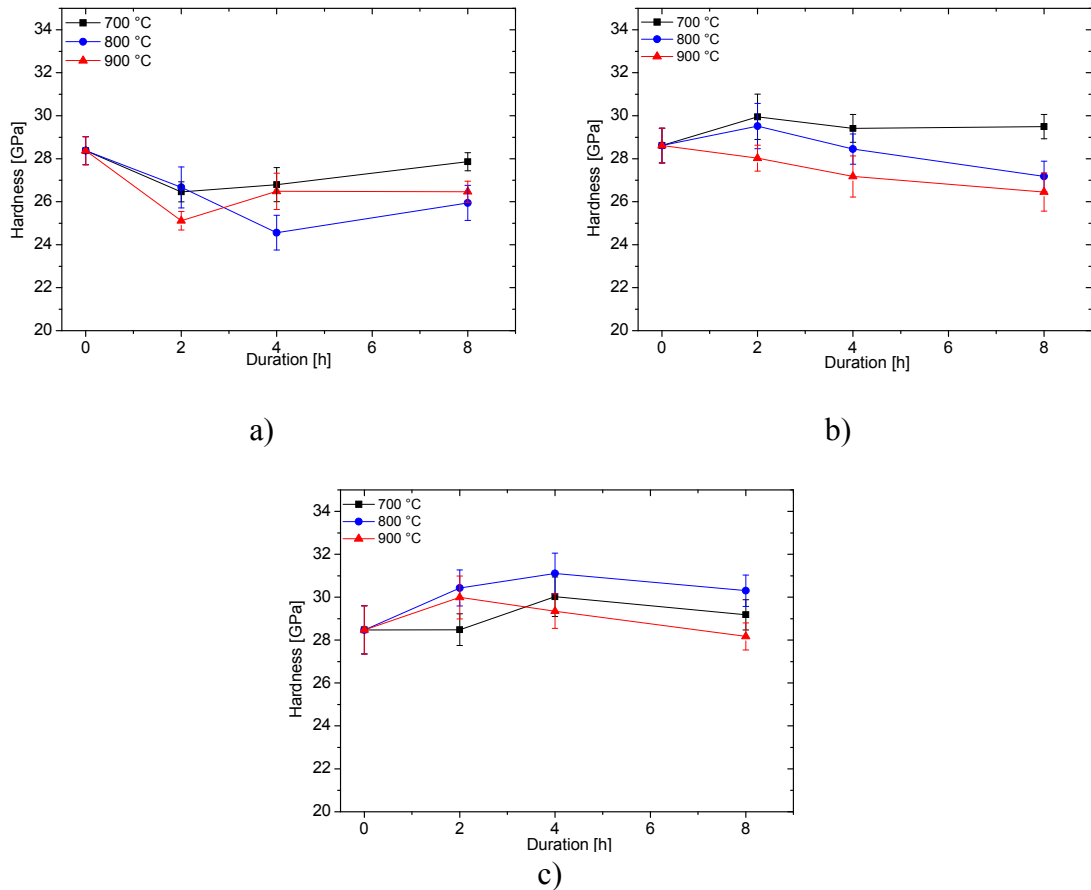
Fig. 32: Hardness of coatings within the constant Ti series annealed for 2, 4 and 8 h at 700, 800 and 900 °C
a) T50C65-10, **b)** T50C50-10, **c)** T50C30-10

Fig. 33 shows the hardness of coatings within the constant Cr series. After annealing at 700 °C, all coatings showed higher hardness values compared to annealing at 800 and 900 °C. An exception is the coating T60C50-10, where the hardness after annealing at 800 °C is higher than at 700 °C. Only after annealing for 8 hours at 700°C, the hardness was significantly increased, whereas after annealing for 8 hours at 800 °C the value remained constant.

After annealing at 800 °C, the hardness of coatings T33C50-10 and T40C50-10 was at ~29 GPa, independent of the annealing duration, see Fig. 33b, c). After annealing at 900 °C, all coatings showed the lowest hardness values. The hardness of the samples T33C50-10 and T40C50-10 decreased with increasing annealing duration. An exception is the coating T40C50-10. It showed an increased hardness value of 27.6 GPa after 8 hours annealing, whereas the coating T60C50-10 showed constant low hardness values.
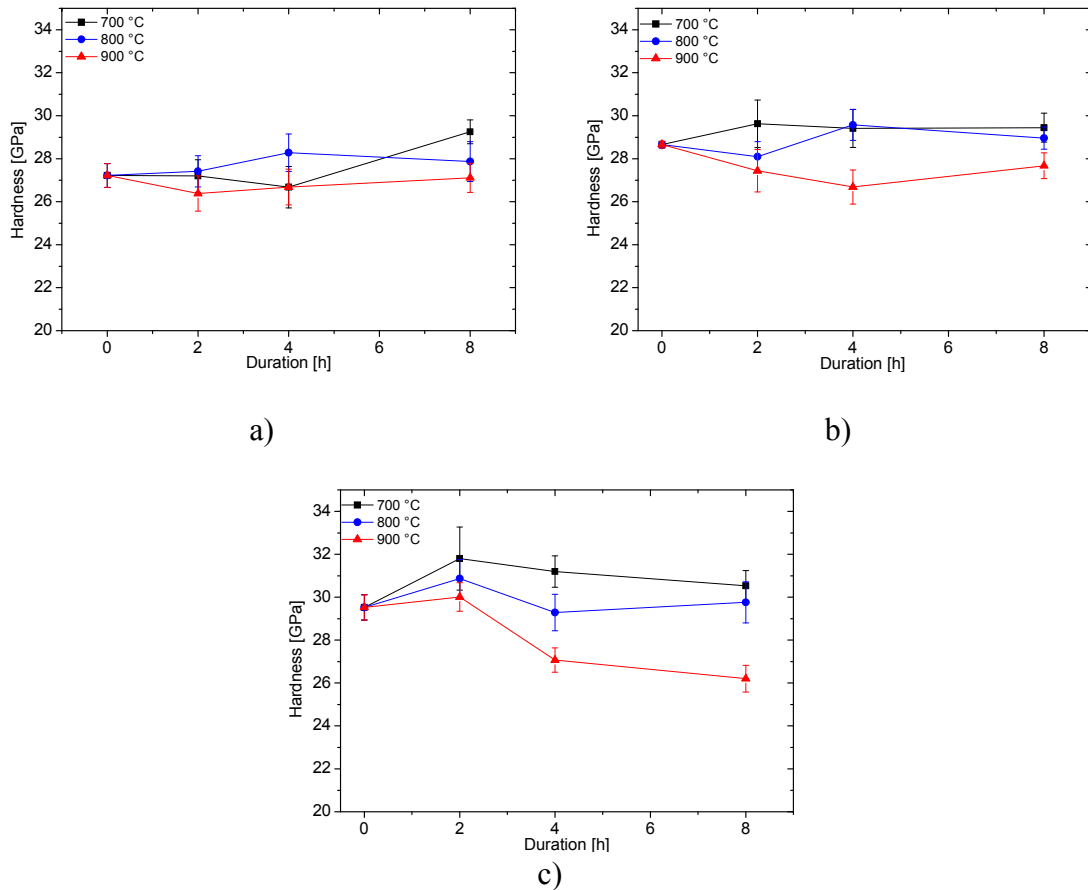
Fig. 33: Hardness of coatings within the constant Cr series annealed for 2, 4 and 8 h at 700, 800 and 900 °C
a) T60C50-10, **b)** T40C50-10, **c)** T33C50-10

4.8 Cutting Performance

The maximum flank wear (mfw) describes the wear of the cutting edge during cutting application. In Fig. 34 a) the mfw values as function of the cutting duration of the coatings with 10 nm layer thickness is shown. One cut represents a cutting time of 13.7 min. Independent of the Al content, all coatings from the constant Ti series showed high wear. T50C65-10 was worn through during the first cut, which is evidenced by a high flank wear. During the second cut, coatings T50C50-10, T50C30-10 and T60C50-10 also failed. In Fig. 34 b) and c) the life time obtained for the constant Ti series and the constant Cr series are illustrated. In the constant Ti series, the sample T50C65-10 has a life time of 1.4 min, whereas the coatings T50C50-10 and T50C30-10 failed after 14.5 min and 14.7 min due to the high wear.

With decreasing Ti content the flank wear decreased. The coating T60C50-10 showed the worst mfw within the constant Cr series surviving only 14.1 min. The samples T33C50-10, T40C50-10 and the reference T50T31.7-10 showed similar mfw values between 0.08 and 0.1 mm until the third cut. After the fourth cut, the mfw of coating T33C50-10 increases significantly to 0.15 mm. In contrast, the values of coating T40C50-10 and the reference

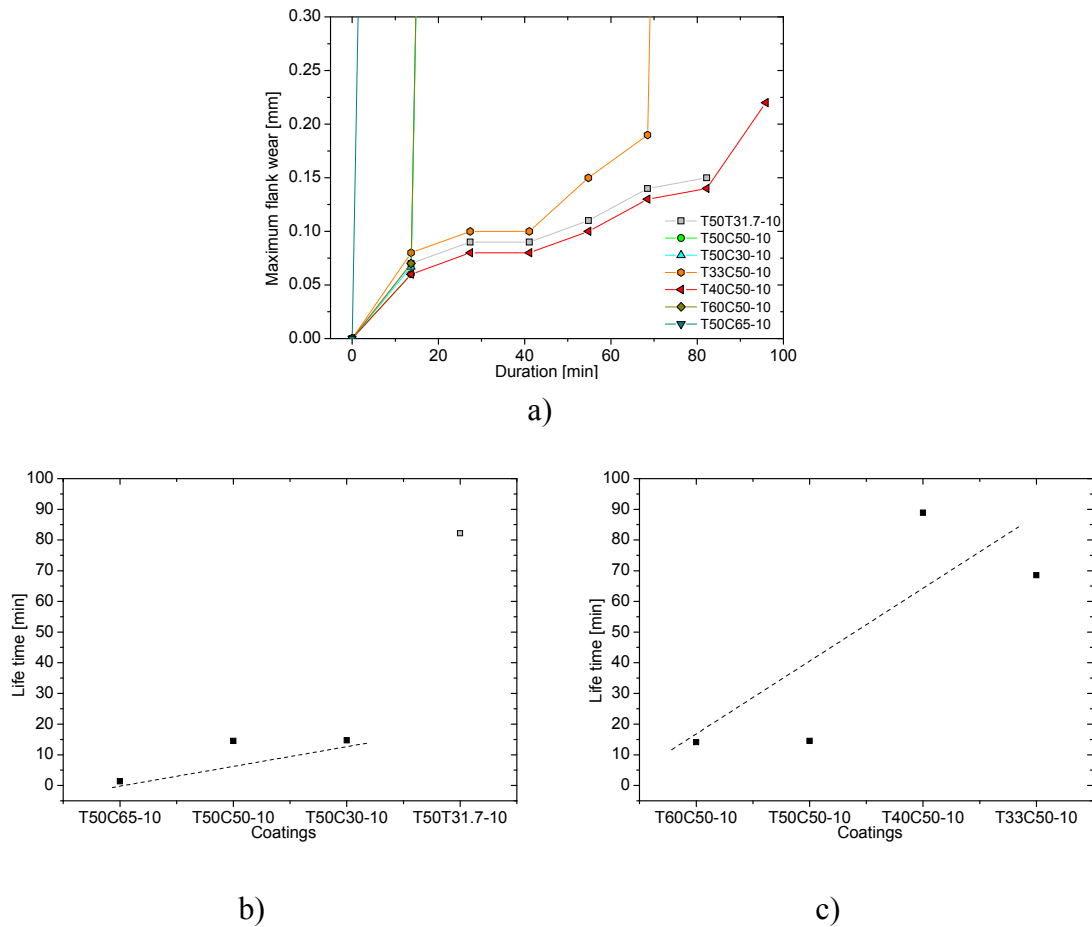showed a lower increase of Δmfw of ~0.02 mm. This tendency was also continued after the fifth cut.

a)

b)

c)

Fig. 34: a) Maximum flank wear as function of the cutting duration for all coatings with layer thickness of 10 nm, **b)** Life time of the constant titanium series, **c)** Life time of the constant chromium series

During the sixth cut T33C50-10 failed after 68.5 min, whereas T40C50-10 showed the lowest mfw of 0.14 mm compared with the value of the reference (0.15 mm). Because of the high number of cracks on the cutting edge, which define the life time (Fig. 35), the test for the reference sample was stopped after the sixth cut. The reference yielded a life time of 82.2 min. After the seventh cut, the mfw of T40C50-10 was significantly increased to 0.22 mm, which exceeds the acceptable wear resulting in termination of the test. T40C50-10 showed with 88.9 min the longest life time of all coatings.
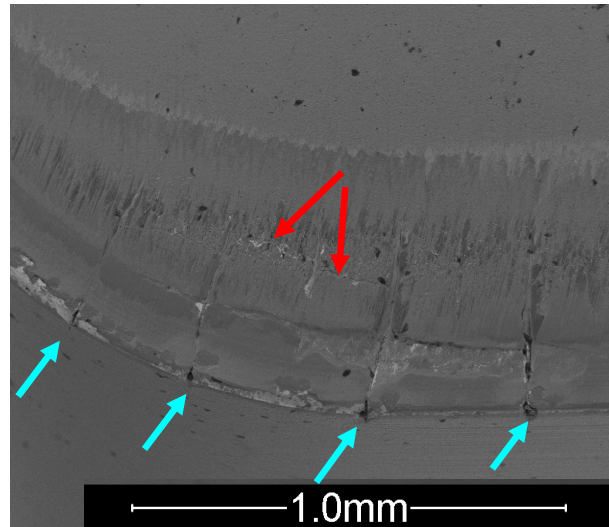
Fig. 35: SEM micrograph of the worn cutting edge of reference coating: Definition the life time by crack formation

Fig. 36 a-c) illustrate the mfw values as function of the layer thickness, and Fig. 36 d) shows the life time dependent on the layer thickness for the different coating compositions. Fig. 36 a) summarizes the mfw values of the T50C30 samples. After the first cut, all coatings showed similar mfw values around 0.7 mm. During the second cut, the coatings with 10, 30 and 100 nm layer thickness failed. The sample T50C30-300 showed a mfw value of 0.9 mm after the second cut. Because of the high number of cracks on the cutting edge, the test had to be stopped, yielding a life time of 27.4 min.

In Fig. 36 b) the performance of the coatings with target composition T50C50 is illustrated. The coating T50C50-300 failed during the first cut and had a life time of only 1.4 min. After the first cut, the other coatings showed an increased mfw value with increasing layer thickness. Independent of the mfw value coating T50C50-10 failed during the second cut and achieved a life time of 14.5 min. With increasing cutting duration, the mfw values of coatings T50C50-30 and T50C50-100 increased slightly. Due to the high number of cracks on the cutting edge, the test of sample T50C50-100 was stopped after the third cut. This coating yielded a life time of 41.1 min. After the fourth cut, coating T50C50-30 showed a significantly increased mfw value of 0.15 mm and during the fifth cut it failed. This coating yielded a life time of 54.8 min.

The life time of coatings with the target composition T33C50 increases with decreasing layer thickness, see Fig. 36 d). All coatings were intact after the first cut. After the second cut, the mfw value of coating T33C50-30 remained nearly constant, whereas for the other coatings the mfw increased at least by Δmfw ~0.02 mm. After the third cut, coating T33C50-30 had a higher mfw value than sample T33C50-10. The mfw value of coating T33C50-300 increased significantly. In contrast, the mfw values of coatings T33C50-10 and T33C50-100 remained nearly constant. During the fourth cut, coating T33C50-300 failed and sample T33C50-100 did not survive because of high numbers of cracks. They yielded the same life time of

41.1 min. After the fourth cut, for sample T33C50-30 the mfw value remained constant at 0.11 mm. During the fifth cut, T33C50-30 failed. The coating yielded a life time of 54.8 min. The mfw value of coating T33C50-10 increased significantly after the third cut and during the sixth cut the milling insert was broken. This coating yielded a life time of 68.5 min.
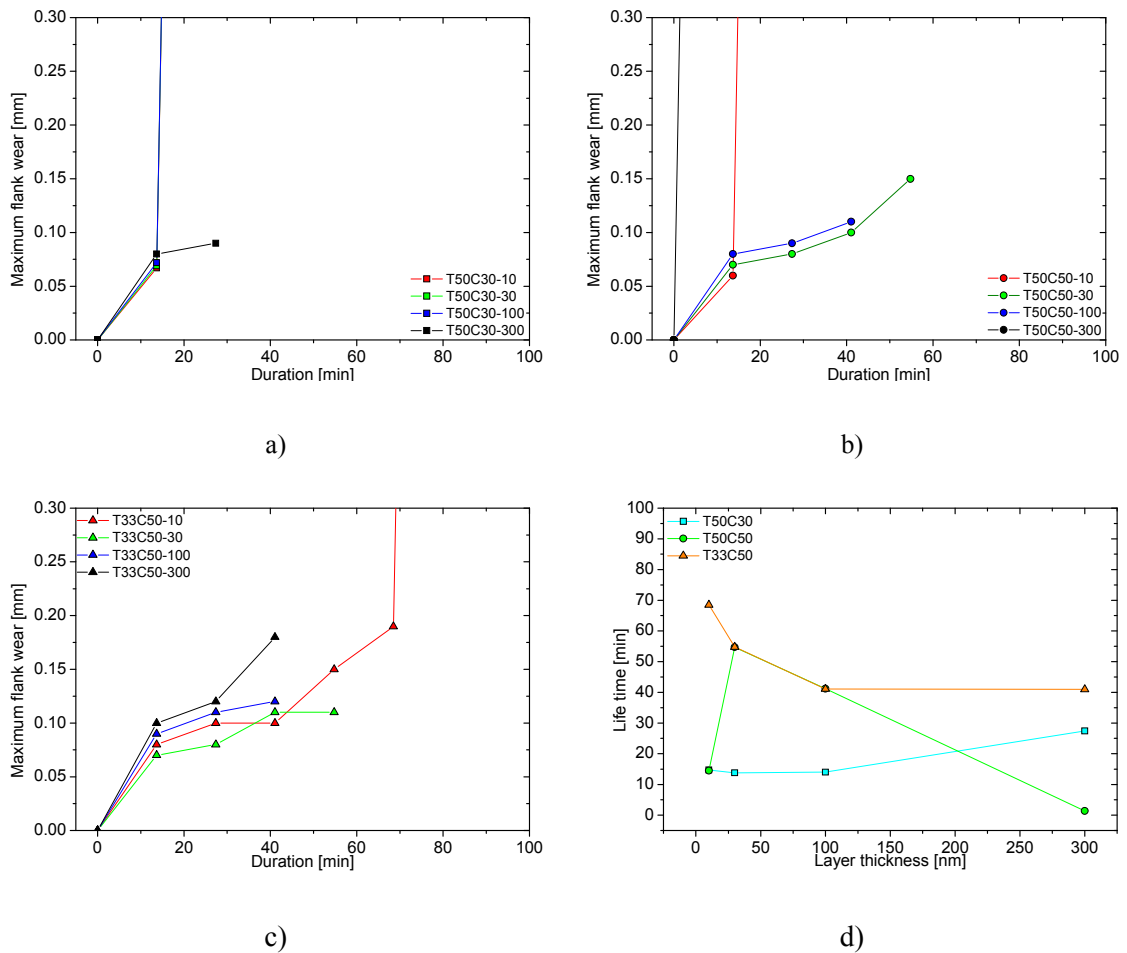

a)

b)

c)

d)

Fig. 36: Maximum flank wear as function of the cutting duration depending on the layer thickness for target compositions **a)** T50C30, **b)** T50C50, **c)** T33C50, **d)** Life time as function of the layer thickness

The SEM micrographs in Fig. 37 show the reference and coating T40C50-10, to illustrate the damage of the milling inserts during the cutting tests. After the first cut, the reference showed a higher number of cracks on the cutting edge than coating T40C50-10. With increasing cutting duration, the cracks grow and get broader. When the critical cutting duration of the reference was yielded, a new crack was created, which ran through other cracks, thus connected them. When the cracks yielded a critical length, the whole cutting edge would break away. The life time of coating T40C50-10 was yielded by flaking off the coating and not by the cracks.
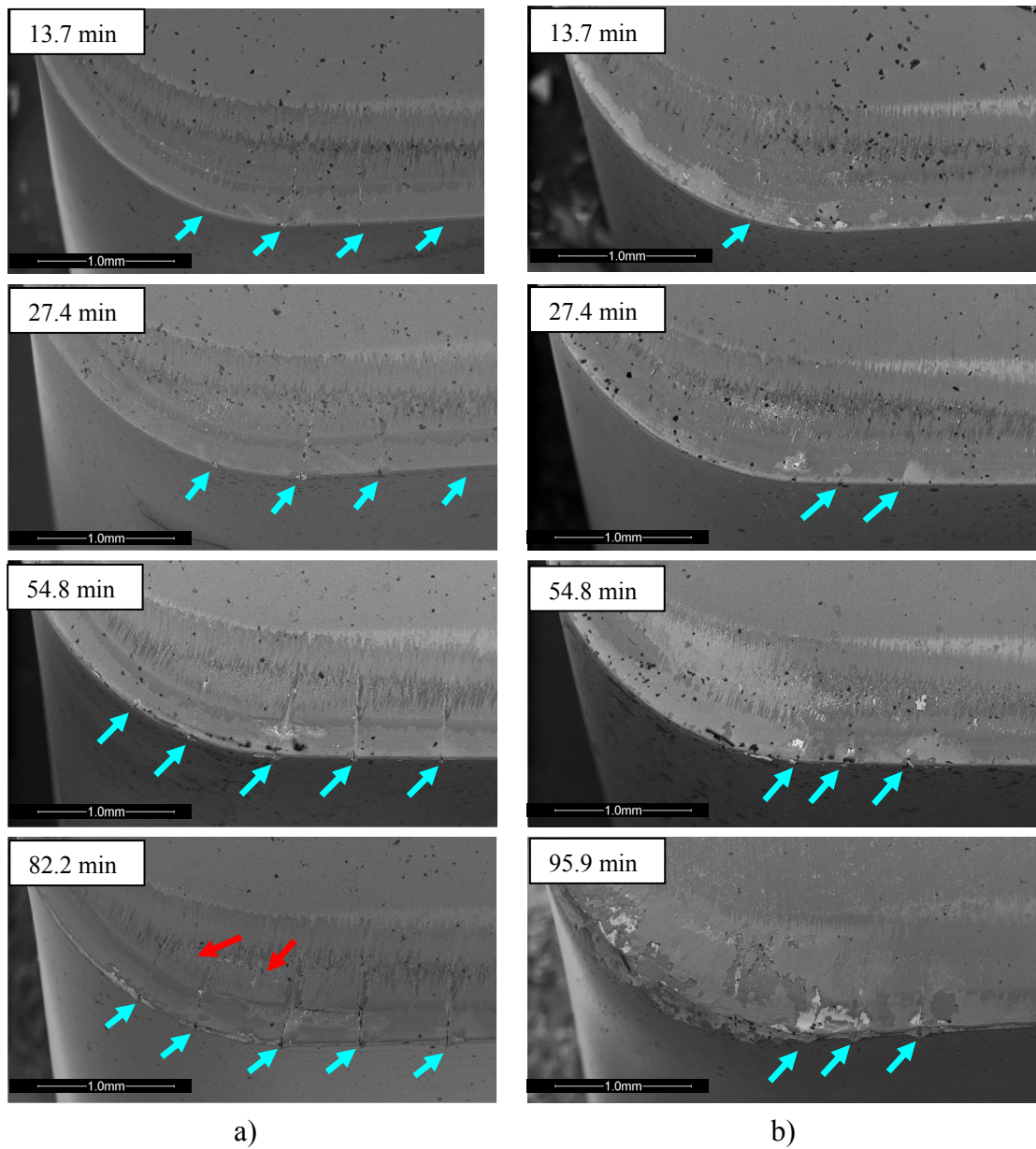
Fig. 37: SEM micrographs of cutting edges of sample **a)** of T50T31.7-10, **b)** T40C50-10 after different cutting durations

5 Discussion

This section discusses the effect of the Al content in the coatings, the lattice misfit between the TiAlN and CrAlN layer and the layer thickness on the mechanical properties and the thermal stability of the developed multilayer coatings. These interpretations provide the basis to explain the results obtained in the cutting tests and illuminate potential directions for further developments.

Fig. 38 gives a schematic illustration of TiAlN/CrAlN bilayer, visualizing two mechanisms for improving the mechanical properties of the multilayer system. According to the literature, the distortion of the fcc lattice of both, TiAlN and CrAlN layers, with increasing Al content, see Fig. 14. Furthermore, the coherency strains between the single layers caused by the lattice misfit can be assumed to affect the mechanical properties [34, 40, 46].
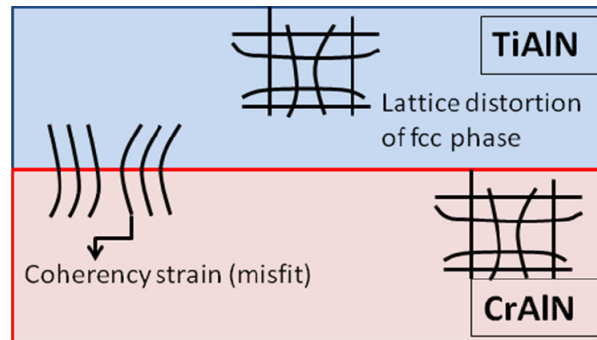

Fig. 38: TiAlN/CrAlN bilayer with illustration of lattice distortion by Al incorporation and coherency strains introduced by the misfit between the layers

One of the major findings of this thesis is that the increased distortion of the fcc lattice by increasing Al content (i.e. within the individual layer) is more efficient in improving the mechanical properties of the coatings than the lattice misfit between the layers. To exemplify, the sample deposited using the target composition $Ti_{0.5}Al_{0.5}/Cr_{0.3}Al_{0.7}$ (i.e. a moderate Al content in the TiAlN and a high Al content in the CrAlN layer) yielded a relatively high hardness of ~28 GPa and also a high lattice misfit. However, a comparably high hardness of ~29 GPa but a low lattice misfit was found for the sample with the target composition $Ti_{0.33}Al_{0.67}N/Cr_{0.5}Al_{0.5}N$, i.e. a high Al content in the TiAlN and a moderate content in the CrAlN layer.

Al incorporation in the TiAlN seems to be more effective than in the CrAlN layer. In particular, the residual compressive stress in the multilayer having an Al rich TiAlN layer, i.e. grown from the $Ti_{0.33}Al_{0.67}/Cr_{0.5}Al_{0.5}$ targets, is ~1000 MPa higher than that for the system with an Al rich CrAlN layer, synthesized using $Ti_{0.5}Al_{0.5}/Cr_{0.3}Al_{0.7}$ targets. These results correspond well to the experimentally verified formation of a metastable solid solution according to Vegard's law [81].

In agreement with the literature [9], the layer thickness also affects the mechanical properties of the multilayer systems. Coatings with low layer thickness of 10 nm show an improved hardness, due to their also reduced grain size. According to the Hall-Petch relationship [72-74], their hardness is increased by hindered dislocation movement due to the high number of interfaces. Furthermore, it is also possible that the coherency strains between the layers contribute to the hardness increase. While coatings with intermediate layer thicknesses have a slightly lower hardness, multilayer arrangements with 300 nm layer thickness also yielded an increased hardness. This can be explained by the more crystalline structure of the thicker layers.

For all coatings, decomposition of the fcc (Ti,Cr)AlN phase into fcc AlN phase, fcc TiN and fcc CrN, hcp AlN phase at eveluated temperature was found. No evidence of formation of the Cr_2N phase was found. The multilayer architecture obviously hinders the further decomposition of the fcc CrN phase, since the TiAlN layers provide an effective barrier against N out-diffusion. In general, the Al rich coatings showed a higher driving force for decomposition. For these coatings, consequently a slightly higher hardness of about +2 GPa was measured after the decomposition process, which occurred between 700 and 800 °C. This hardness increase is based on the developing coherency strains between the formed precipitations in the matrix [61-65, 82].

In excellent agreement to the effects described above, for the multilayer arrangements based on target compositions $Ti_{0.33}Al_{0.67}/Cr_{0.5}Al_{0.5}$ and $Ti_{0.4}Al_{0.6}/Cr_{0.5}Al_{0.5}$, i.e. with an Al rich TiAlN layer, and a layer thickness of 10 nm the best performance in the cutting tests was obtained.

6 Conclusions and Outlook

6.1   Conclusions

Within this thesis, TiAlN/CrAlN multilayers for cemented carbide cutting inserts were deposited by cathodic arc evaporation from TiAl and CrAl targets with different chemical compositions, i.e. $0.33 \leq Ti \leq 0.6$ and $0.30 \leq Cr \leq 0.6$. Different layer thicknesses, i.e. (10, 30, 100, and 300 nm) have been investigated. All coatings are characterized by epitaxial layer growth. The Al content within the coatings is lower than in the targets, due to pronounced scattering of Al during transport from target to substrate. All coatings showed solely the fcc TiAlN or CrAlN phase, respectively. The Al in the TiAlN layer has a more pronounced influence on residual stress and hardness, whereas it had only a minor effect in the CrAlN layers. For multilayer arrangements with layer thicknesses of 10 or 300 nm, respectively, the highest hardness was obtained. Annealing of the coatings in the temperature range between 700 and 800 °C resulted in decomposition of the metastable TiAlN and CrAlN phases in face centered cubic AlN and TiN or CrN, respectively. Formation of these precipitations resulted in a slight hardness increase for Al-rich coatings. For annealing temperatures above 900 °C, also the hexagonal AlN phase could be detected. Coatings with 10 nm layer thickness and the highest Al content investigated yielded the best performance in the milling test.

6.2   Outlook:

For the future, an investigation of two topics seems to be promising:

- Variation of the layer thickness and Al content: There, the TiAlN layer thickness should be adjusted in the range between 10 and 30 nm, whereas for CrAlN it should be chosen around 5 nm. Al rich TiAlN layer are characterized by significantly higher hardness compared to CrAlN, whereas an Al rich CrAlN layer should provide an enhanced oxidation resistance. To avoid a negative effect of this CrAlN layer, it should be considerably thinner than the TiAlN layer.

- Investigation of multilayered TiAlN/TiAlTaN coatings with CrAlN: Multilayered coatings based on TiAlN and TiAlTaN layers are presently state of the art in cutting applications and have been investigated within this thesis as a reference material. A promising approach could be the improvement by the addition of Al rich CrAlN layers, to form an architecture consisting of three individual layers.

7 References

[1]   K.W. Mertz, H.A. Jehn, Praxishandbuch moderne Beschichtungen, Fachbuchverlag Leipzig, Leipzig, 2001

[2]   H. Jehn, Keimbildung und Wachstum dünner Schichten, H. Fischermeister and H. Jehn (Eds.) in Hartstoffschichten zur Verschleißminderung, DGM, Oberursel, (1987), 45

[3]   Handbuch der Gewindetechnik und Frästechnik, Emuge Franken, Publicis Corporate Publishing, 2004

[4]   P.H. Mayrhofer, Vorlesungsskriptum Basics of Deposition & Materials Science of Hard Coatings, Montanuniversität Leoben, Leoben, 2011

[5]   K. Kutschej, Wear resistant, low friction hard coatings for cutting applications, Ph.D. thesis, Montanuniversität Leoben (2005)

[6]   C. Mitterer, P.H. Mayrhofer, M. Beschliesser, P. Losbichler, P. Warbichler, F. Hofer, P.N. Gibson, W. Gissler, H. Hruby, J. Musil, J. Vlček Surf. Coat. Technol., 120- 121 (1999), 405

[7]   H.A. Jehn, B. Rother, J. Refract. Metals Hard Mater., 14 (1996), 87

[8]   J. Patscheider, T. Zehnder, M. Diserens, Surf. Coat. Technol., 146 −147 (2001), 201

[9]   H. Holleck, V. Schier, Surf. Coat. Technol., 76- 77 (1995), 328

[10] S. Zhang, D. Sun, Y. Fu, H. Du, Surf. Coat. Technol., 167 (2003), 113

[11] J. Musil, Surf. Coat. Technol., 125 (2000), 322

[12] M. Zhou, Y. Makino, M. Noose, K. Nogi, Thin Solid Films, 339 (1999), 203

[13] W. Kalss, A. Reiter, V. Derflinger, C. Grey, J.L. Endrino, Int. J. Refract. Metals Hard Mater., 24 (2006), 399

[14] M. Zhu, M. Li, Y. Zhou, Surf. Coat. Technol., 201 (2006), 2878

[15] D.M. Mattox, Handbook of Physical Vapor Deposition (PVD) Processing, Noyes Publication, 1998

[16] B. Rother, J. Vetter, Plasmabeschichtungsverfahren und Hartstoffschichten, Deutscher Verlag für Grundstoffindustrie, Leipzig, 1992

[17] R. F. Bunshah, S. M. Rossnagel, G. E. McGuire (eds.), Handbook of Hard Coatings, Deposition Technologies, Properties and Applications, Noyes Publications, New Jersey (2001), p. 4

[18] W.D. Münz, D. Hoffmann, Metalloberfläche, 37 (1983), 7

[19] H. Frey, Vakuumbeschichtung 1, Plasmaphysik und Plasmadiagnostik, Analytik, VDI-Verlag, Düsseldorf, 1995

[20] W. Gissler, H.A. Jehn, Advanced Techniques for Surface Engineering, Kluwer Academic Publishers, Dordrecht 1992

[21]   C.L.Chang, W. Chen, P. Tsai, W. Ho, D. Wang, Surf. Coat. Technol., 202 (2007), 987

[22]   J.L. Vossen, W. Kern, Thin Film Processes II, Academic Press, San Diego, 1991

[23]   Fr.W. Bach, T. Duda, Moderne Beschichtungsverfahren, Wiley-VCH, Weinheim, 2000

[24]   M. Bußmann, K. Möhwald, Beschichtungen aus der Dampfphase, Fr.- W. Bach and T. Duda (Eds.) in Moderne Beschichtungsverfahren, Wiley-VCH, Weinheim, p. 199- 222

[25]   W.-D. Münz, I. Smith, D. Lewis, S. Creasey, Vacuum, 48 (1997), 473

[26]   A. Anders, Surf. Coat. Technol., 120- 121 (1999), 319

[27]   P. Barna, M. Adamik, Thin Solid Films, 317 (1998), 27

[28]   J.A. Thornton, Rev. Mater. Sci., 7 (1977), 239

[29]   B. A. Movchan, A.V. Demchishin, Fiz. Metallov Metalloved., 28 (1969), 653

[30]   A.P. Messier, R.A. Giri, J. Roy, Vac. Sci. Technol., A2 (1984), 500

[31]   H.C. Barshilia, B. Depthi, N. Selvakumar, A. Jain, K. S. Rajam, App. Surf. Sci., 253 (2007), 5076

[32]   A.E. Reiter, C. Mitterer, B. Satory, J. Vac. Sci. Technol., A25 (2007), 711

[33]   H. Willmann, Al-Cr-N thin film design for high temperature applications, Ph.D. thesis, Montanuniversität Leoben (2007)

[34]   A.E. Reiter, V.H. Derfinger, B. Hanselman, T. Bachmann, B. Sartory, Surf. Coat. Technol., 200 (2005), 2114

[35]   H. Willmann, P.H. Mayrhofer, P. Persson, A.E. Reiter, L. Hultman, C. Mitterer, Scripta Mater., 54 (2006), 1847

[36]   P.H. Mayrhofer, H. Willmann, A.E. Reiter, Symposium Society of Vacuum Coaters, 505 (2006), 575

[37]   A. Aubert, R. Gillet, A. Gaucher, J.P. Terrat, Thin Solid Films, 108/2 (1983), 165.

[38]   O. Knotek, W. Bosch, M. Atzor, W.D. Münz, D. Hoffman, J. Goebel, High Temp.– High Press. 18/4 (1986), 435.

[39]   A.E. Reiter, AlCrN coatings: Structure, properties and application potentials, Ph.D. thesis, Montanuniversität Leoben (2009)

[40]   K. Kutschej, P.H. Mayrhofer, M. Kathrein, P. Polcik, R. Tessadri, C. Mitterer, Surf. Coat. Technol., 200 (2005), 2358

[41]   A.E. Santana, A. Karimi, V.H. Derflinger, A. Schütze, Surf. Coat. Technol., 177- 178 (2004), 334

[42]   T. Ikeda, H. Satoh, Thin Solid Films, 195 (1991), 99

[43]   Powder Diffraction File (Card 11-0065 for CrN), International Centre for Diffraction Data, ICDD - JCPDS, 1998.

[44]   D. Gall, C.S. Shin, T. Spila, M. Odén, M.J.H. Senna, J.E. Greene, I. Petrov, J. Appl. Phys., 91/6 (2002), 3589

[45]   J.C.A. Batista, C. Godoy, V.T.L. Buono, A. Matthews, Mater. Sci. Eng., A336 (2002), 39–51

[46]   A. Kimura, H. Hasegawa, K. Yamada, T. Suzuki, Surf. Coat. Technol., 120- 121 (1999), 438

[47]   A. Kimura, M. Kawate, H. Hasegawa, T. Suzuki, Surf. Coat. Technol., 169- 170, (2003), 367

[48]   V. Derflinger, H. Brändle, H. Zimmermann, Surf. Coat. Technol., 113 (1999), 286

[49]   P. Shum, W. Tam, K. Li, Z. Zhou, Y. Shen, Wear, 257 (2004), 1030

[50]   S. Jiang, D. Peng, X. Zhao, L. Xie, Q. Li, App. Surf. Sci., 84 (1995), 373

[51]   H. Holleck, Surf. Coat. Technol., 36 (1988), 151

[52]   E. Santana, A. Karimi, V. H. Derflinger, A. Schütze, Thin Solid Films, 469-470, (2004), 339

[53]   P.H. Mayrhofer, H. Clemens., C. Mitterer, Int. J. Mater. Res., 96 (2005), 468

[54]   Z.J. Lui, P. W. Shum, Y.G. Shen, Thin Solid Films, 468 (2004), 161

[55]   H. Hasegawa, A. Kimura, T. Suzuki, Surf. Coat. Technol., 132 (2000), 76

[56]   M. Okumiya, M. Griepentrog, Surf. Coat. Technol., 112 (1999), 123

[57]   J.L. Endrino, G.S. Fox- Rabinovich, C. Gey, Surf. Coat. Technol., 200 (2006), 6840

[58]   J. Romero, M.A. Gómez, J. Esteve, F. Montalà, L. Carreras, M. Grifol, A. Lousa, Thin Solid Films, 515 (2006), 113

[59]   A. Kimura, H. Hasegawa, Surf. Coat. Technol., 200 (2005), 2409

[60]   O. Knotek, R. Elsing, G. Krämer, F. Jungblut, Surf. Coat. Technol., 46 (1991), 265

[61]   P.H. Mayrhofer, A. Hörling, L. Karlsson, J. Sjölèn, T. Larsson, C. Mitterer, L. Hultman, App. Phys. Lett., 83 (10) (2003), 2049

[62]   M. Stueber, H. Holleck, J. Alloys Compd., 483 (2009), 321

[63]   P. H. Mayrhofer, C. Mitterer, L. Hultman, H. Clemens, Progr. Mater. Sci., 51 (2006) 1032

[64]   T. Göbel, S. Menzel, M. Hecker, W. Brückner, K. Wetzig, C. Genzel, Surf. Coat. Technol., 142- 144 (2001), 861

[65]   A. Hörling, L. Hultman, M. Oden, J. Sjölen, L. Karlsson, J. Vac. Sci. Technol., A20 (2002), 1815

[66]   S. PalDey, S.C. Deevi, Mater. Sci. Eng., A 342 (2003), 58

[67]   H. Ichimura, A. Kawana, J. Mater. Res., 8 (1993), 1093.

[68]   D. McIntyre, J.E. Greene, G. Hakansson, J.E. Sundgren, W.D. Münz, J. Appl. Phys., 67 (1990), 1542.

[69]   K. Chakrabarti, J. Jeong, S. Hwang, Y. Yoo, C. Lee, Thin Solid Films, 406 (2002), 159

[70]   J.L. Endrino, G.S. Fox-Rabinovich, A.E. Reiter, S.V. Veldhuis, R. Escobar Galindo, J.M. Albella, J.F. Marco, Surf. Coat. Technol., 201 (2007), 4505

[71]   M. Kawate, A.K. Hashimoto, T. Suzuki, Surf. Coat. Technol., 165 (2003), 163

[72]   J. E. Sundgren, J. Birch, G. Hakansson, L. Hultman, U. Helmersson, Thin Solid Films, 193-194 (1990), 881

[73] P.H. Mayrhofer, C. Mitterer, Recent Res. Devel. Vac. Sci. Tech. 4, Transworld
      Research Network, 2003, 71

[74] P.H. Mayrhofer, F. Kunc, J. Musil, C. Mitterer, Thin Solid Films, 415 (2002), 151

[75] S. J. Bull, A.M. Jones, Surf. Coat. Technol., 78 (1996), 173

[76] X.M. Xu, J. Wang, J. An, Y. Zhao, Q.Y. Zhang, Surf. Coat. Technol., 201 (2007),
      5582

[77] O. Knotek, F. Löffler, C. Barimani, G. Krämer, Mater. Sci. Forum, 246 (1997), 29

[78] H. Hahn, K.A. Padmanabhan, Nanostruct. Mater., 6 (2005), 191

[79] W.C. Oliver, P.G. M., J. Mater. Res., 7/6 (1992), 1564

[80] R. Franz, B. Sartory, R. Kaindl, R. Tessadri, A. Reiter, V.H. Derflinger, P. Polcik, C.
      Mitterer, in G. Kneringer et al, Proc. 16th Int. Plansee Seminar, Reutte, 2005, 932

[81] L. Vegard, Z. Physik, 5 (1921), 17

[82] H. Willmann, P. H. Mayrhofer, L. Hultman, C. Mitterer, I. Heat Treat. Surf. Engineer,
      1 (2007), 75

8 Appendix

<u>TEM micrographs:</u>

20-21 nm

50 nm

a)

19-21 nm

50 nm
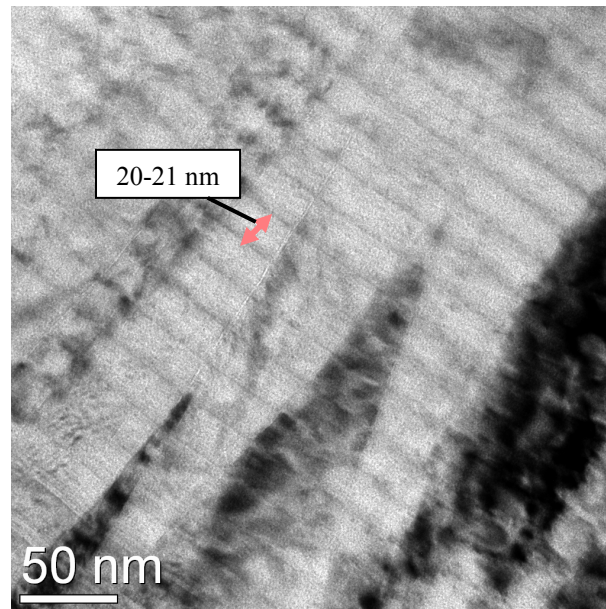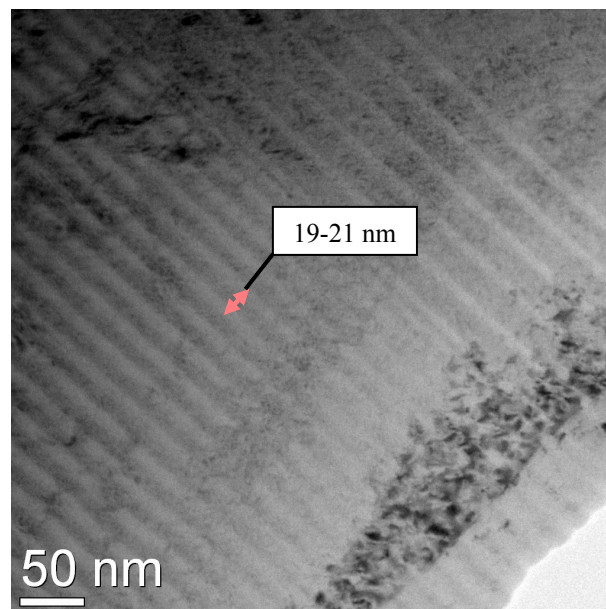
b)

Fig. 39: TEM bright field images of the layer architecture of the coatings **a)** T60C50-10, **b)** T50C65-10

XRD Patterns:
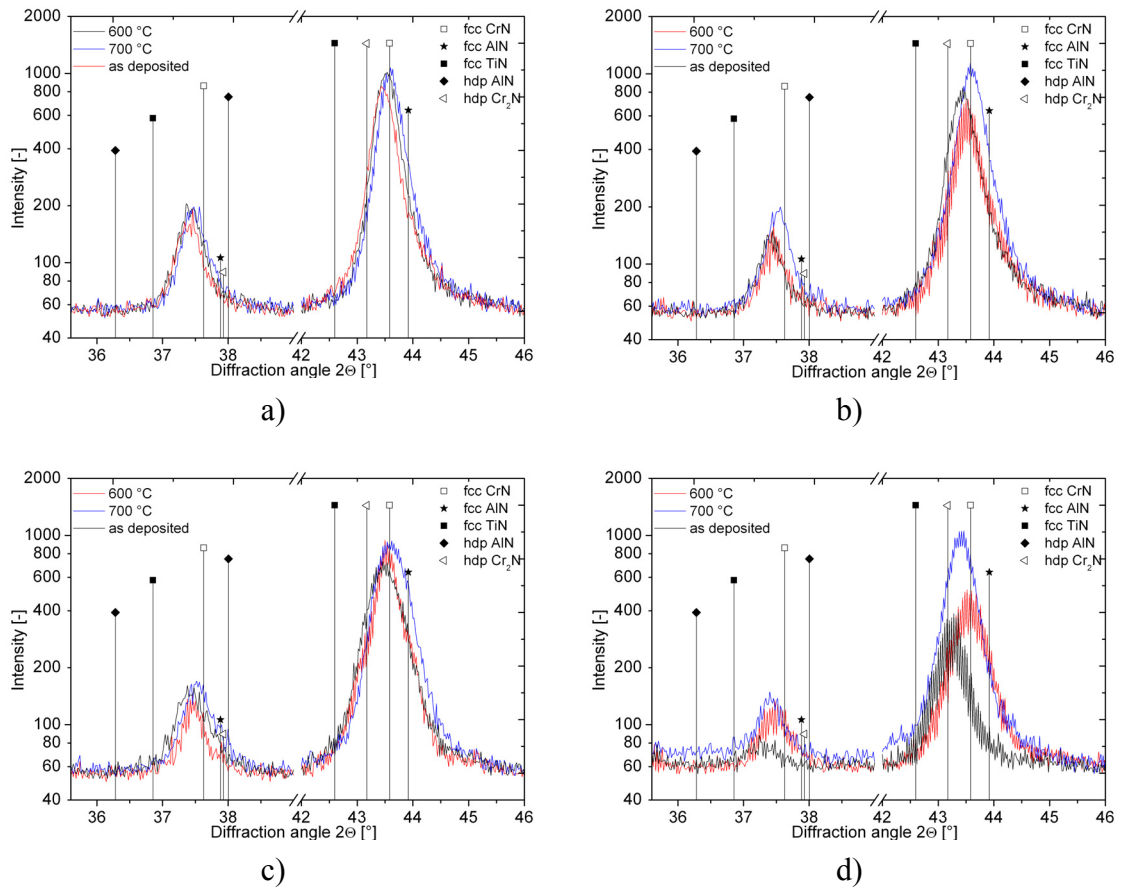
Fig. 40: XRD patterns of coatings **a)** T50C65-10, **b)** T50C50-10, **c)** T50C30-10, **d)** the reference sample T50T31.7-10 annealed at 600 and 700 °C for 2 h compared to the as-deposited state
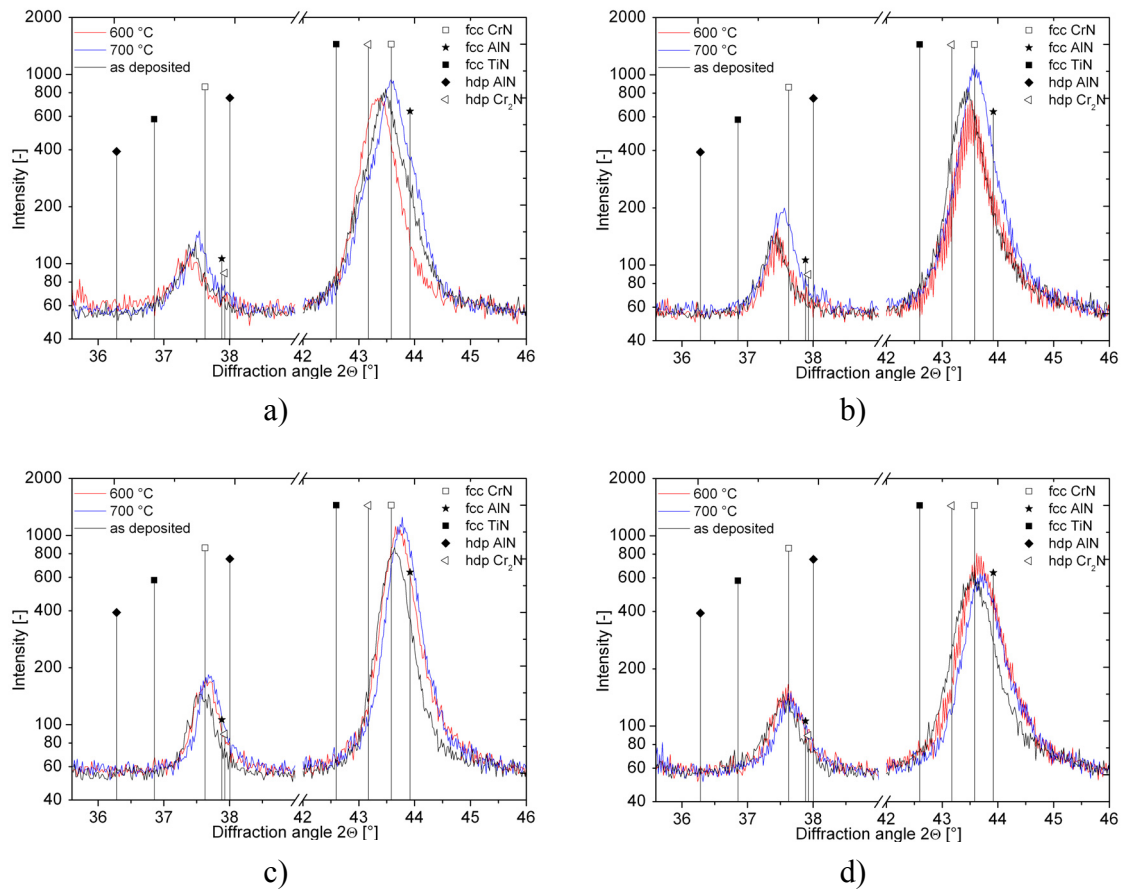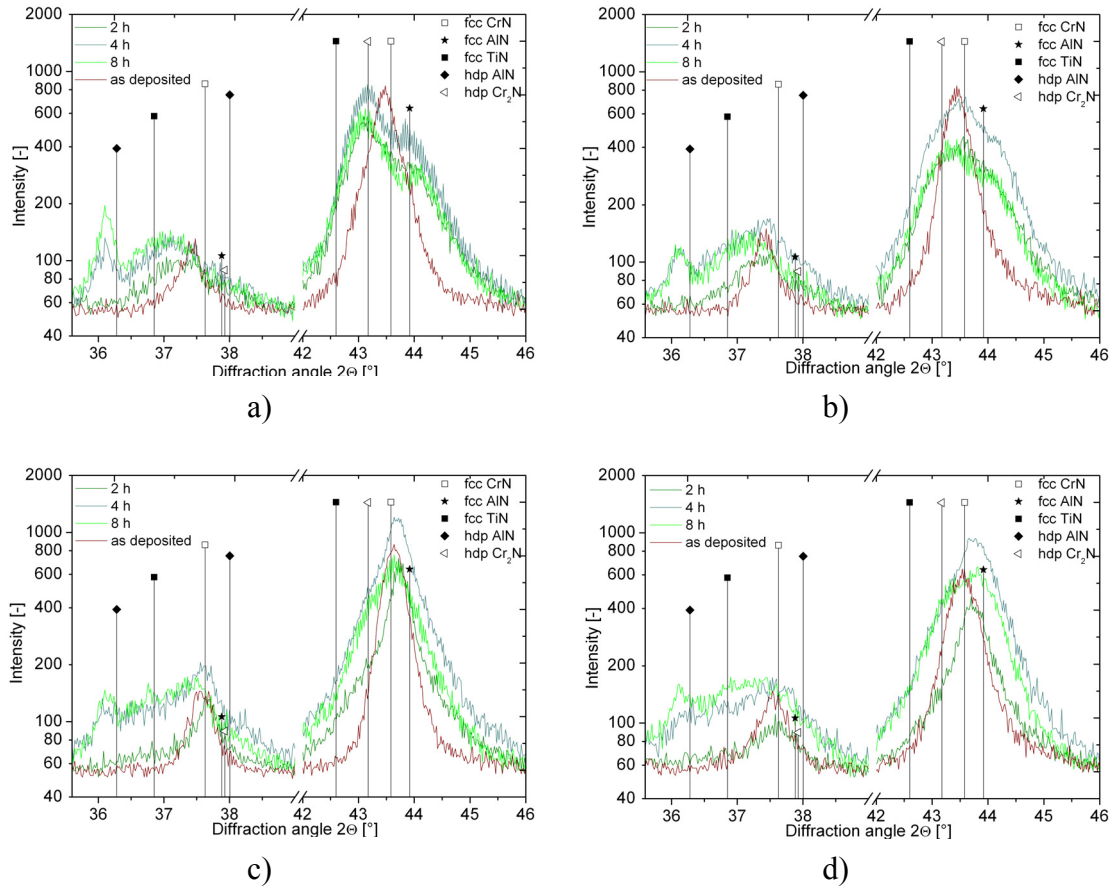
Fig. 41: XRD patterns of coatings **a)** T60C50-10, **b)** T50C50-10, **c)** T40C50-10, **d)** T33C50-10 annealed at 600 and 700 °C for 2 h compared to the as-deposited state
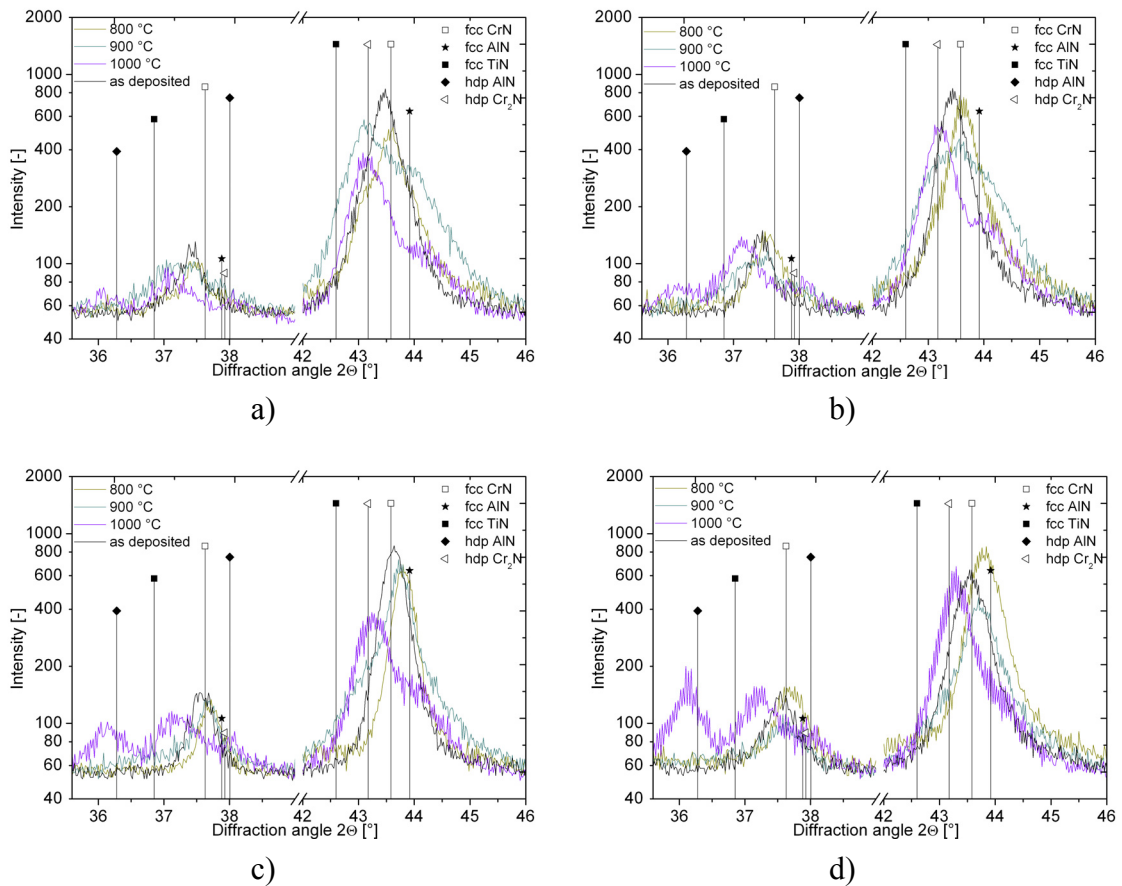
Fig. 42: XRD patterns of coatings **a)** T60C50-10, **b)** T50C50-10, **c)** T40C50-10, **d)** T33C50-10 annealed at 800, 900 and 1000 °C for 2 h compared to the as-deposited state
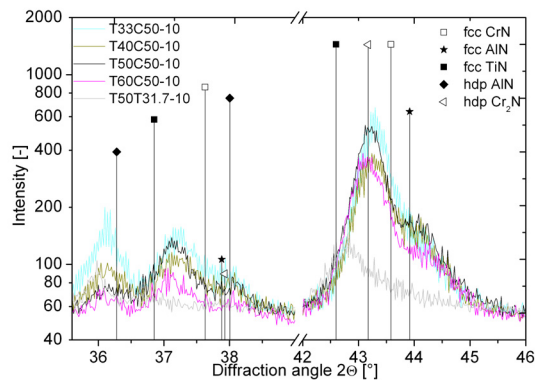
Fig. 43: Comparison of the coatings T33C50-10, T40C50-10, T50C50-10, T60C50-10 and the reference sample T50T31.7-10 annealed at 1000 °C for 2 h

Fig. 44: XRD patterns of coatings **a)** T60C50-10, **b)** T50C50-10, **c)** T40C50-10, **d)** T33C50-10 annealed at 900 °C with annealing duration of 2, 4 and 8 h and compared to the as-deposited state
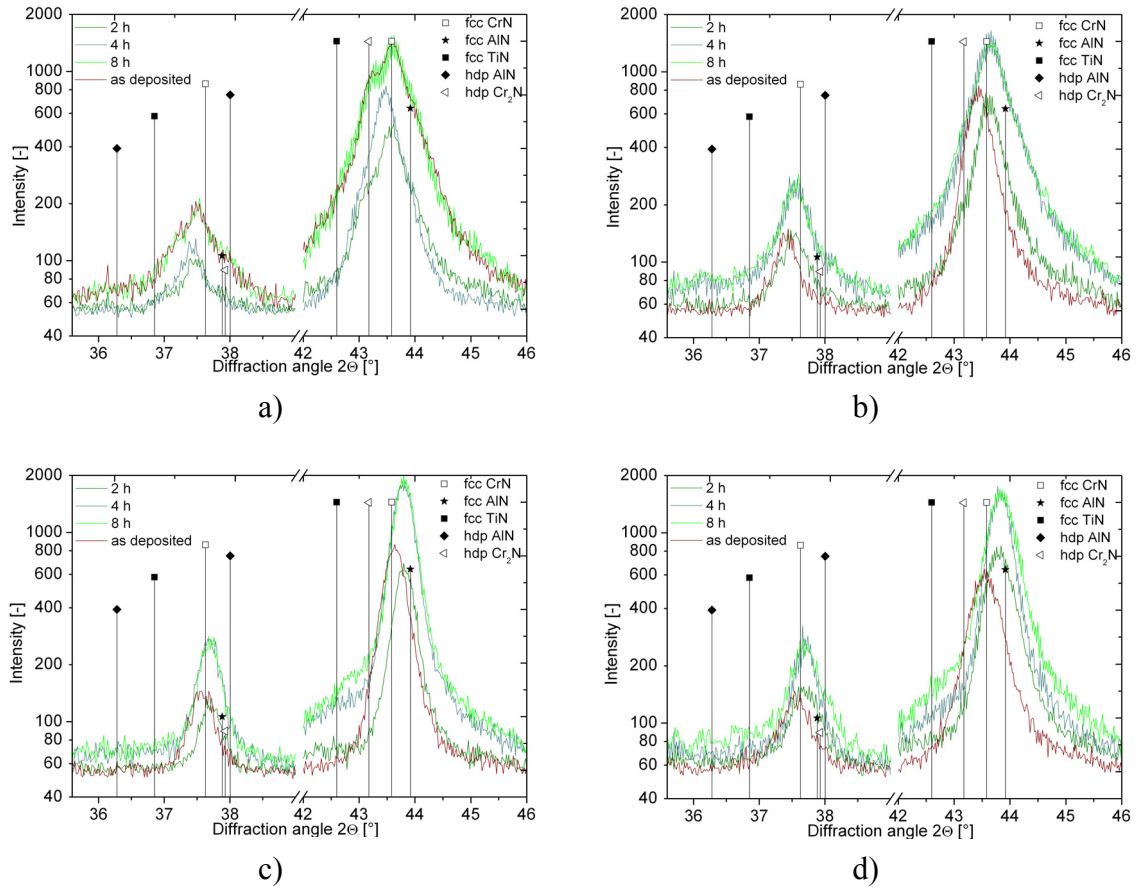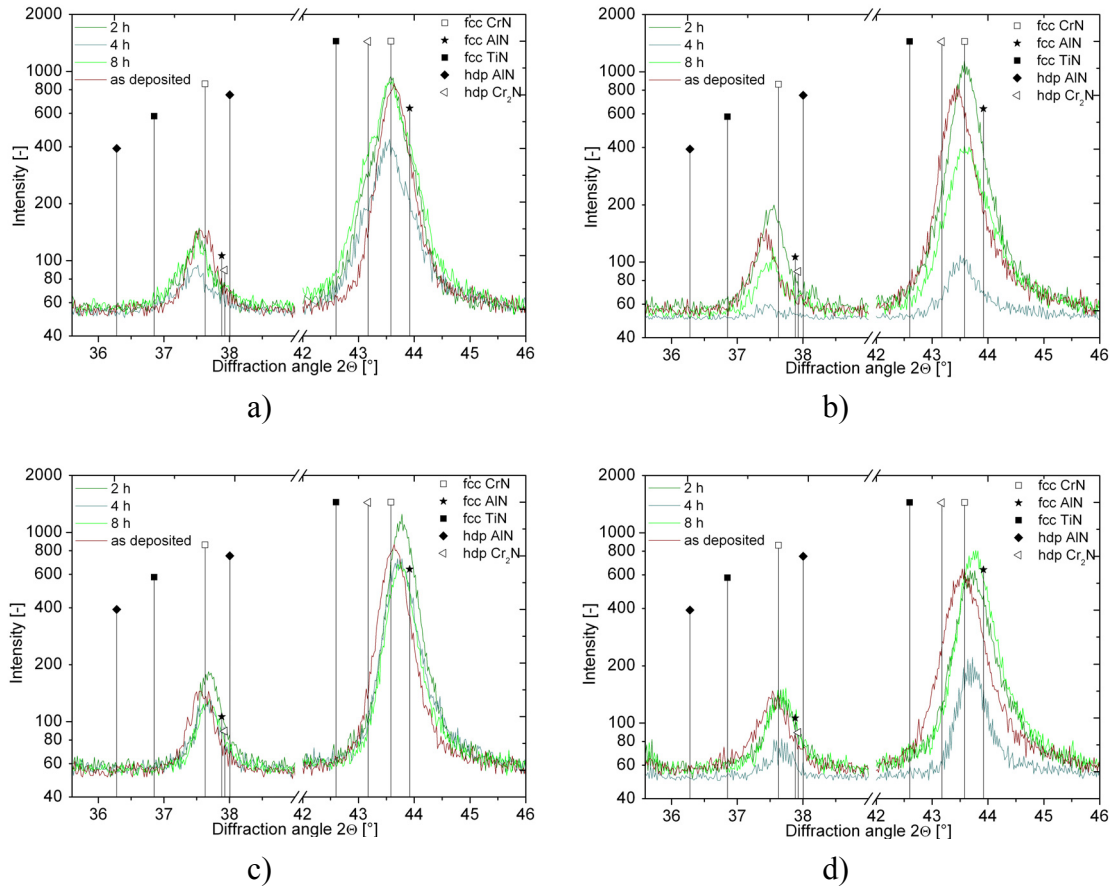
Fig. 45: XRD patterns of coatings **a)** T60C50-10, **b)** T50C50-10, **c)** T40C50-10, **d)** T33C50-10 annealed at 800 °C with annealing duration of 2, 4 and 8 h and compared to the as-deposited state

Fig. 46: XRD patterns of coatings **a)** T60C50-10, **b)** T50C50-10, **c)** T40C50-10, **d)** T33C50-10 annealed at 700 °C with annealing duration of 2, 4 and 8 h and compared to the as-deposited state
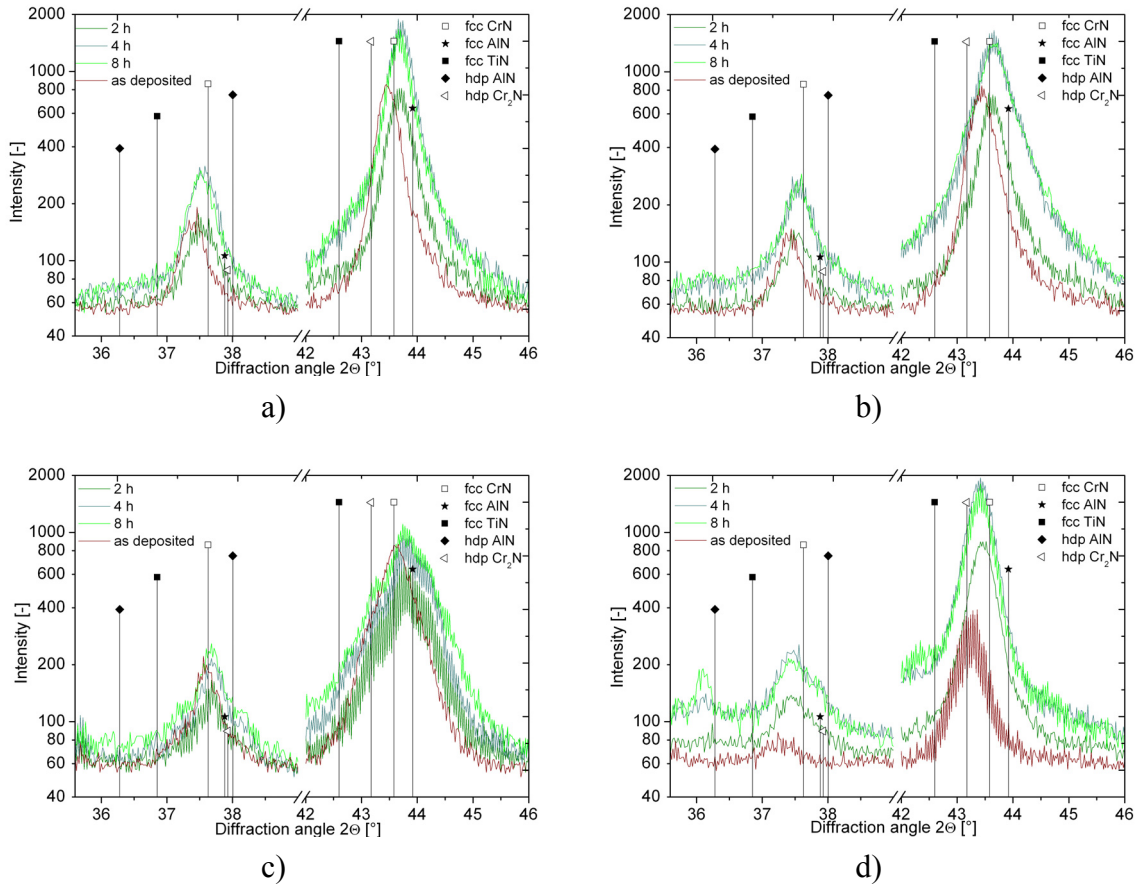
Fig. 47: XRD patterns of coatings **a)** T50C65-10, **b)** T50C50-10, **c)** T50C30-10, **d)** the reference sample T50T31.7-10 annealed at 800 °C with annealing duration of 2, 4 and 8 h and compared to the as-deposited state
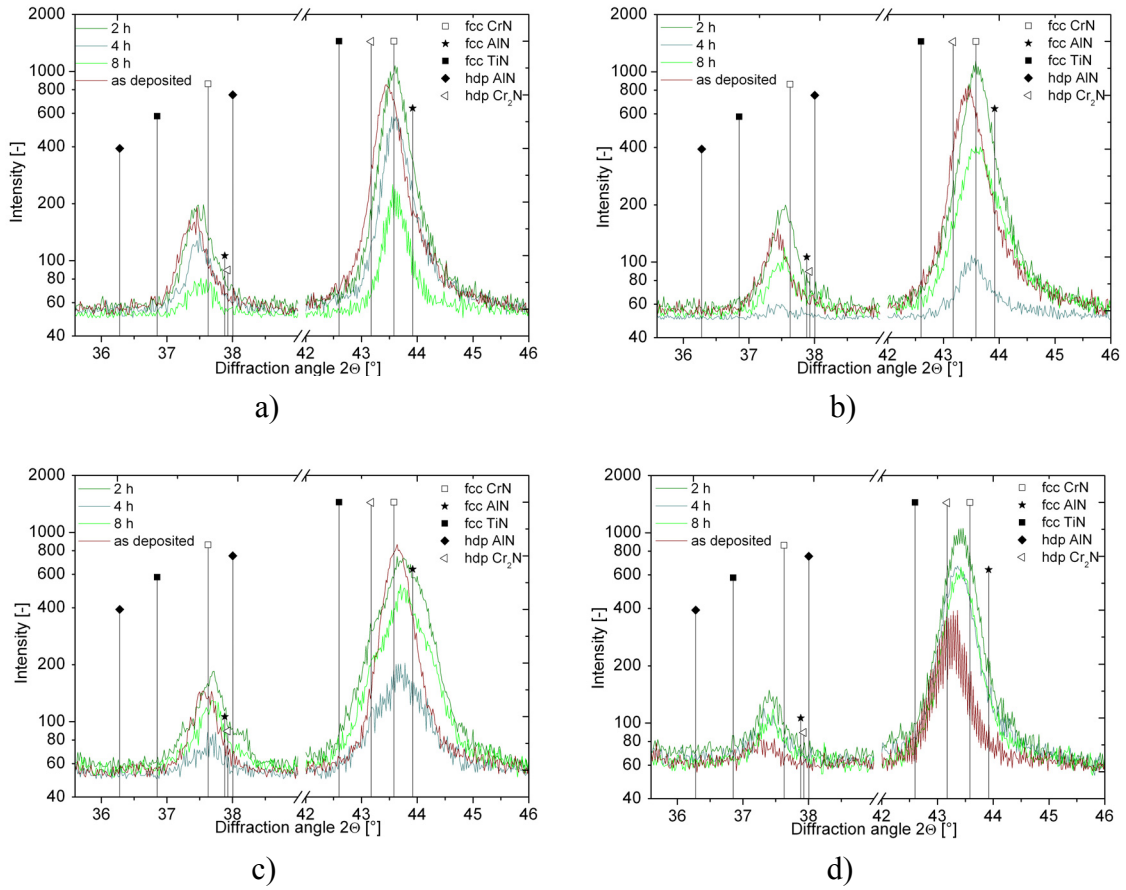
Fig. 48: XRD patterns of coatings **a)** T50C65-10, **b)** T50C50-10, **c)** T50C30-10, **d)** the reference sample T50T31.7-10 annealed at 700 °C with annealing duration of 2, 4 and 8 h and compared to the as-deposited state